Structural, electronic, and dynamical properties of carbon nanomaterials

vorgelegt von
Diplomphysiker
Nils Rosenkranz
aus Ulm

von der Fakultät II - Mathematik und Naturwissenschaften
der Technischen Universität Berlin
zur Erlangung des akademischen Grades

Doktor der Naturwissenschaften
– Dr. rer.nat. –

genehmigte Dissertation

Promotionsausschuss:

Vorsitzender:	Prof. Dr. Michael Lehmann
Berichter:	Prof. Dr. Christian Thomsen
	Prof. Dr. Milan Damnjanović

Tag der wissenschaftlichen Aussprache: 14.5.2013

Berlin 2013
D 83

Zusammenfassung – German abstract

In dieser Arbeit untersuchen wir verschiedene niederdimensionale Kohlenstoffstrukturen mittels *ab initio* und semi-empirischen Berechnungen. Die Arbeit gliedert sich in zwei Teile. Zunächst beschäftigen wir uns mit Picotube Molekülen sowie deren Verhältnis zu Kohlenstoff Nanotubes. Im zweiten Teil wird der Einfluss von mechanischer Verspannung einerseits sowie Funktionalisierung andererseits auf die Materialeigenschaften von Graphen untersucht.

Picotubes sind hoch-symmetrische, ringförmige Kohlenwasserstoffe, die Substrukturen von armchair Nanotubes darstellen. Wir zeigen, dass sich die strukturelle Ähnlichkeit beider Materialsysteme in den Eigenschwingungen widerspiegelt. Erstens weisen Picotubes und Nanotubes optische Schwingungsmoden bei ähnlichen Frequenzen auf. Weiterhin finden wir in allen untersuchten Picotubes radiale Atmungsmoden, deren Frequenzen wie im Falle von Nanotubes indirekt proportional zum Durchmesser sind. Aufgrund der weitgehenden Analogien zwischen beiden Strukturen gelten Picotubes als Ausgangspunkt für eine potentielle gezielte Synthese sortenreiner Nanotubes. Wir widmen uns dieser Fragestellung mit molekulardynamischen Simulationen von in Nanotubes eingefüllten Picotubemolekülen. Abhängig von der simulierten Temperatur zeigen unsere Berechnungen Oszillationen sowie eine kontinuierliche axiale Bewegung der Picotubes im Nanotube. Bei Temperaturen über 2500 K führen chemische Umwandlungen zu einer Transformation der Picotubestruktur in eine kurze, geschlossene Röhre. Insbesondere das zuletzt genannte Ergebnis ist im Hinblick auf eine mögliche Herstellung definierter Nanotubes von großer Bedeutung.

Im zweiten Teil beschäftigen wir uns mit Graphen Nanoribbons. Mechanische Verspannung sowie die Art der Passivierung der Randatome haben einen großen Einfluss auf die elektronischen Eigenschaften und die Phononen von Nanoribbons. Die Bandlücke von verspannten armchair Nanoribbons vergrößert oder verkleinert sich je nach dem, welcher Familie der Nanoribbon gemäß der gängigen Klassifikation angehört. Dieses Phänomen lässt sich konsistent im Sinne früherer Arbeiten zu verspanntem Graphen interpretieren. Dasselbe gilt für die Frequenzen der wichtigsten Schwingungsmoden, die alle eine Verschiebung zu kleineren Werten zeigen. Unter dem Einfluss einer Funktionalisierung der Ränder mit Hydroxylgruppen beobachten wir zum Teil ähnliche Effekte. Wir zeigen, dass sich die Bandlücke funktionalisierter Nanoribbons einerseits durch Verspannung, aber auch durch eine Änderung der Quantisierungsbedingung der elektronischen Wellenfunktionen ändert. Des Weiteren untersuchen wir die energetischen Verschiebungen charakteristischer Phononen. Unsere Daten legen die Möglichkeit nahe, den Grad der Funktionalisierung in Raman Experimenten zu bestimmen. Insbesondere die starke Abhängigkeit der Bandlücke von potentiell einstellbaren äußeren Faktoren könnte sich in zukünftigen nanoelektronischen Anwendungen als nützlich erweisen.

Abstract

In this work we study a variety of low-dimensional carbon structures by means of *ab initio* and semi-empirical calculations. The thesis comprises two main parts. The first one deals with picotube molecules and their relation to carbon nanotubes. In the second part, we investigate how strain and edge functionalization affect the fundamental properties of graphene nanoribbons.
Carbon picotubes are a class of highly symmetric, ringlike hydrocarbons which closely resemble short sections from armchair nanotubes. We demonstrate that this structural analogy leads to typical vibrational characteristics of nanotubes being inherited onto picotubes. Apart from optical modes found in the same frequency range as in nanotubes, picotubes exhibit radial-breathing modes as well. We find the frequency of this mode to depend inversely on the picotube diameter in accordance with the relation known from carbon nanotubes. Owing to the close relation of both carbon allotropes picotubes are considered suitable starting points for a controlled synthesis of nanotubes. We address this issue by molecular dynamics simulations of picotubes encapsulated in nanotubes in a peapod-like configuration. Our temperature-dependent studies reveal three independent effects. Besides oscillations of the picotubes in the nanotube and a continuous molecular transport along its axis we observe a transformation of the picotube structure into a tubular form at temperatures around 2500 K. The latter result might be a step along the path to a bottom-up synthesis of specific types of nanotubes.
Another form of fascinating one-dimensional carbon materials besides nanotubes are graphene nanoribbons. The second part of this thesis covers uniaxial strain and hydroxyl edge passivation in armchair nanoribbons. The electronic and vibrational properties of these ribbons prove to be highly sensitive to both of the mentioned modifications. We find the band-gap of strained nanoribbons to strongly increase or decrease depending on the family armchair nanoribbons are commonly classified in. These shifts, which are linear in a large strain range, can be interpreted in terms of earlier reports on the band structure of uniaxially strained graphene. The main vibrational modes of nanoribbons show a severe red-shift under tensile strain which can be related to corresponding studies on graphene as well. Introducing hydroxyl edge passivation leads to partially comparable effects since the ribbon structure is strained upon this type of functionalization. We successfully explain the observed band-gap energies of hydroxylized nanoribbons by a combination of strain effects and a modified effective confinement condition for the electronic wave functions. Finally we present data on prominent phonons including specific vibrations of the hydroxyl groups which suggest that the degree of functionalization may be determined in Raman experiments. Especially our findings on tunable band-gap energies by applying strain or attaching functional edge groups might be of significant technological relevance in future nano-electronic applications.

List of publications

Ab initio calculations of edge-functionalized armchair graphene nanoribbons: Structural, electronic, and vibrational effects,
N. Rosenkranz, C. Till, C. Thomsen, and J. Maultzsch,
Phys. Rev. B **84**, 195 438 (2011).

Uniaxial strain in graphene and armchair graphene nanoribbons: An *ab initio* study,
N. Rosenkranz, M. Mohr, and C. Thomsen,
Ann. Phys. **523**, 137 (2011).

Molecular Dynamics Simulations of Picotube Peapods,
N. Rosenkranz and C. Thomsen,
Phys. Status Solidi B **246**, 2622 (2009).

Vibrational properties of four consecutive carbon picotubes,
N. Rosenkranz, M. Machón, R. Herges, and C. Thomsen,
Phys. Status Solidi B **245**, 2145 (2008).

Vibrational properties of semitrimer picotubes,
N. Rosenkranz, M. Machón, R. Herges, and C. Thomsen,
Chem. Phys. Lett. **451**, 2145 (2008).

Contents

1 Introduction

Elemental carbon occurs in a large variety of allotropes. The two basic crystalline phases of bulk carbon, diamond and graphite, differ in the configuration of the atomic valence shells. In diamond, all valence electrons occupy sp^3 hybrid orbitals leading to a tetrahedral bonding pattern. A graphitic plane, by contrast, has a flat hexagonal crystal structure which results from the hybridization of the s orbital with only two out of three p orbitals. Whereas in both cases neighboring carbon atoms form strong covalent bonds, the inter-planar coupling in a graphite crystal is given by the relatively weak van der Waals interaction.

Both of the electronic configurations mentioned above are also found in carbon nanostructures, *i.e.*, in structures with one or more dimensions being limited to the nanometer range. The most prominent sp^3 hybridized nanomaterials are small sections of a diamond crystal with hydrogen-terminated surfaces referred to as diamondoids [1,2]. While these hydrocarbons have a molecular character, the sp^2 configuration, in addition, permits one- and two-dimensional crystalline structures, all of which can be deduced from a single graphitic plane. The first sp^2-like nanostructures to be discovered were the fullerenes [3]. In these cage-like spherical molecules certain hexagons are replaced by pentagons enabling a biaxial curvature. Apart from coiling a graphitic sheet into a sphere, one could also imagine rolling it into a hollow cylinder. The resulting carbon nanotubes, which were first discovered in 1991, typically have a large aspect ratio and can therefore be considered to be quasi one-dimensional [4]. The underlying material of these structures, a single sheet from a graphite crystal, is referred to as graphene. It was isolated in 2004 by Novoselov *et al.* in a remarkably simple approach [5]. Another class of one-dimensional substructures of graphene which became accessible thereby is given by narrow stripes from a graphene sheet, the so-called graphene nanoribbons.

The availability of the nanostructures described above has triggered enormous research efforts in this field. Reducing a dimension to the order of a nanometer introduces quantum confinement and thus induces fundamentally new phenomena compared to bulk materials. Besides the pure scientific ambition to explore new physics, the huge interest in these materials is driven by the prospect of exploiting their fascinating properties in a wide range of potential applications. In particular, carbon nanotubes as well as graphene combine a wealth of outstanding characteristics. Extreme values have been reported on their mechanical stabilities, their low mass densities, and their high thermal conductivities, to name a few [6–9]. The most intriguing aspect, however, is the peculiar band structure of graphene, which is inherited in a modified version onto carbon nanotubes. This leads, amongst other effects, to extraordinarily high electronic mobilities of graphene and nanotubes suggesting a carbon-based miniaturization of electronic devices [10–12].

Graphene does not have a band-gap which would be necessary in many applications like transistors. Here, carbon nanotubes can serve as complementary building blocks. One peculiarity of nanotubes is that slight changes in their geometrical structure determine whether an actual tube is semiconducting or metallic [13]. Therefore, an important goal is either to synthesize nanotubes in a controlled manner or sort the mixtures in the outputs of typical production processes. Although various separation techniques allow the enrichment of nanotubes of a certain diameter or according to their metallicity, none of these methods provide a way to obtain tubes of a defined diameter and chirality up to now [14, 15]. An entirely different approach aims for a controlled bottom-up synthesis of specific types of carbon nanotubes starting from ring-shaped hydrocarbons [16]. These fully conjugated molecules which closely resemble short sections of nanotubes are referred to as carbon picotubes [17]. The nature of these molecules and their relation to carbon nanotubes form the first part of this thesis.
Similar to the case of nanotubes the lateral confinement in graphene nanoribbons introduces a band-gap [18, 19]. Therefore, nanoribbons may potentially complement nanotubes in future electronic devices. However, it should be noted that the electron mobility is expected to be reduced in ribbons compared to that in nanotubes and graphene [20]. Whereas some concepts of carbon nanotubes can be transferred to nanoribbons, the edges represent an additional crucial factor which strongly affects the basic properties of nanoribbons. The band-gap has been shown to depend on the edge type as well as on the ribbon width. Thus, a precise control of these parameters is required in the production process of nanoribbons in order to make use of them in nano-electronic applications. Whereas lithographic methods leave problems comparable to those encountered when manufacturing nanotubes, the chemical synthesis of a specific type of nanoribbon in a bottom-up approach has recently been reported [21]. Although this is a significant step forward in nanoribbon research some vital issues still have to be clarified. One open question concerns the effect of strain in graphene nanoribbons which can arise, for example, due to lattice mismatch if the ribbon is deposited on some arbitrary substrate. Another vital issue is the type of passivation of the dangling edge bonds. Previous reports show that different edge configurations strongly influence the characteristics of the ribbon [22–24]. Apart from a simple reconstruction, the high reactivity of the edges enhances the probability of functional groups being attached to the ribbon edges. In the second part of this work, we address these questions by investigating the influence of uniaxial strain as well as the effect of hydroxyl groups attached to the ribbon edges. It turns out that both topics are closely correlated.
This thesis is organized as follows. We first review our approaches to simulate the properties of the nanostructures described above in Chap. 2. We make use of *ab initio* methods in our studies of isolated picotube molecules and graphene nanoribbons. In addition, semi-empirical calculations are employed in order to simulate the dynamical behavior of compound systems including a large number of atoms. In Chap. 3, we demonstrate the close analogy of carbon pico- and nanotubes with respect to their structural and vibrational properties. Furthermore, the interaction between both allotropes is investigated in a configuration which possibly facilitates the transformation of picotubes into closed nanotube sections. To this end, we arrange a series of picotubes along the axis of a nanotube

in analogy to fullerene peapods [25]. Different aspects of the temperature-dependent dynamics of this system are discussed in Chap. 4. Our findings are in accordance with a previous work pointing to a reorganization of encapsulated picotubes towards tubular structures which is a remarkable result in the light of a potential controlled synthesis of carbon nanotubes, one of the big goals in nanotube research [26].
The following three chapters are devoted to another one-dimensional carbon system, graphene nanoribbons. After reviewing their basic properties in Chap. 5 we investigate how the electronic band structure and characteristic phonons of nanoribbons are affected by strain. The band-gap variations and phonon shifts are then discussed in the context of previous studies on strained graphene (see Chap. 6). Chapter 7 deals with hydroxyl functionalization of nanoribbon edges. We concentrate on nanoribbons with so-called armchair edges as functionalization of these structures has hardly been considered in the literature. It turns out that, beyond effects reported on other types of functionalized nanoribbons, further issues like a functionalization-induced deformation of the ribbon itself play an important role. In this picture, we thoroughly discuss the impact of hydroxyl passivation on the electronic spectrum and the phonon frequencies. The main results of this thesis are summarized in Chap. 8.

2 Computational methods

2.1 Ab initio calculations

Ab initio approaches aim for a description of the physical properties of molecules and solids by means of purely quantum mechanical methods while excluding the use of experimentally derived parameters. The basic simplification of the full many-body hamiltonian is the Born-Oppenheimer approximation which seperates the treatment of the electrons from that of the ions due to the large mass ratio of both particles [27]. Since the remaining electronic hamiltonian is still impractical to solve directly, several approaches have been developed which constrict the ansatz of the many-body electronic wave function. For example, the electrons are decoupled within the Hartree approximation. This ansatz has the disadvantage of not satisfying the Pauli exclusion principle. A possible way to overcome this problem is to express the all-electron wave function as a slater determinant which is referred to as Hartree-Fock method. In both approaches, applying the variational method leads to quasi one-particle equations for the different orbitals. The methods mentioned above have in common that the principle approximation to the electronic wave function is introduced *before* finding the ground state by variation of the energy. Since in both approaches the ansatz does not span the whole Hilbert space of possible solutions of the Schrödinger equation, the true ground state can not necessarily be reached. This fundamental problem can be solved by considering the density as the basic variable as described in the following.

2.1.1 Density functional theory

In 1964, Hohenberg and Kohn demonstrated that the ground state density $n_0(\boldsymbol{r})$ of a many body system uniquely determines its hamiltonian [28, 29]. In particular, the electronic ground state wave function can be expressed as a functional of the density

$$\Psi_0(\boldsymbol{r}_1, ..., \boldsymbol{r}_N) = \Psi[n_0(\boldsymbol{r})], \tag{2.1}$$

where N is the number of electrons. This implies that all observables are functionals of $n_0(\boldsymbol{r})$ as well. Hence, the ground state energy can now be obtained as

$$E_0 = \min_{n \to n_0} \Big\{ T[n(\boldsymbol{r})] + U[n(\boldsymbol{r})] + V[n(\boldsymbol{r})] \Big\}. \tag{2.2}$$

$T[n(\boldsymbol{r})]$ and $U[n(\boldsymbol{r})]$ denote the kinetic energy and the electron-electron potential, respectively. Both functionals are universal in the sense that they do not depend on the external potential of the nuclei $v(\boldsymbol{r})$ which defines the specific system. $V[n(\boldsymbol{r})]$ is the

expectation value of $v(\boldsymbol{r})$

$$V(\boldsymbol{r}) = \int d^3r n(\boldsymbol{r}) v(\boldsymbol{r}). \tag{2.3}$$

Equation 2.2 shows that the energy is now to be minimized with respect to 3 coordinates instead of 10^{23} variables of the wave functions in typical solids. Carrying out the explicit variation of the total energy functional results in effective single-particle equations

$$\left\{ -\frac{\hbar^2}{2m}\nabla^2 + v_{eff}(\boldsymbol{r}) \right\} \varphi_j = \epsilon_j \varphi_j. \tag{2.4}$$

Note that $v_{eff}(\boldsymbol{r})$ depends on the solutions φ_j, hence the term 'effective' one-particle equation. These equations have the same form as those found in the Hartree and Hartree-Fock methods. While the Hartree ansatz neglects exchange and correlation between the electrons the Hartree-Fock approach includes the exchange interaction by satisfying the Pauli principle, but still excludes correlation. In contrast, density functional theory allows a formally exact treatment of the electronic interaction by introducing the so-called exchange-correlation energy E_{xc} [30]. Kohn and Sham suggested to summarize all contributions that are not covered by the kinetic energy of non-interacting particles and the mean-field Coulomb interaction in E_{xc}. The resulting effective potential in Equ. 2.4 takes the form

$$v_{eff}(\boldsymbol{r}) = v(\boldsymbol{r}) + \frac{e^2}{4\pi\epsilon_0} \int d\boldsymbol{r'} \frac{n(\boldsymbol{r'})}{|\boldsymbol{r} - \boldsymbol{r'}|} + v_{xc}(\boldsymbol{r}), \tag{2.5}$$

where the second term on the right-hand side is the mean-field Coulomb energy, *i.e.*, the Hartree energy. In practice, the set of equations 2.4 is solved iteratively until a self-consistent set of $n(\boldsymbol{r})$ and $v_{eff}(\boldsymbol{r})$ is found. Strictly speaking, the eigenvalues of the Kohn-Sham equations ϵ_j do not have a direct physical meaning. Nevertheless, they are often interpreted as the true electronic energy states of the given system, which proves to be a reasonable approximation since they are consistent with the correct electron density [31].

Up to this point, no approximation has been introduced into the density-functional approach. However, the universal functional $E_{xc}[n(\boldsymbol{r})]$ is unknown. Considering a series expansion of $E_{xc}[n(\boldsymbol{r})]$ the simplest approximation is that of a locally constant electron density. In this picture the functional can be written as

$$E_{xc} = \int d\boldsymbol{r}\ e_{xc}(n) n(\boldsymbol{r}). \tag{2.6}$$

Since $n(\boldsymbol{r})$ is assumed to be constant here, e_{xc} does not depend on a function, but on the scalar variable n. The function $e_{xc}(n)$ is identical for every system. In the limits of low and high densities it has been determined already prior to the developement of the density-functional theory [32, 33]. In 1981, the function was calculated also in the intermediate range by means of Monte-Carlo simulations [34].

The concept of a locally constant $e_{xc}(n)$ is known as the local-density approximation (LDA). Although it is a rough description of the real physical situation the method

gives surprisingly precise results and is therefore widely used in the computation of a broad range of material properties. The accuracy of the LDA depends on how much the real electron distribution differs from a homogeneous electron liquid. Hence, metals are particularly well described within this approach. For semiconducting and isolating materials, which involve localized electronic states, it has been shown that the LDA underestimates the band-gaps. A correction to the electron-electron interaction based on the Green's functions formalism, which fixes these discrepancies, was suggested by Hybertsen and Louie [35].
All *ab initio* calculations in this work have been derived by means of the density-functional theory in the LDA. We do not take into account corrections to E_{xc} as we believe that the effects investigated here are not affected by a scaling of the energy levels.

2.1.2 The SIESTA code

The density-functional theory has been implemented in a variety of codes. Besides different approaches being used to evaluate the exchange-correlation energy, the codes differ in the type of basis functions chosen to describe the Kohn-Sham eigenvectors. The DFT calculations presented in this thesis have been carried out with the help of the SIESTA code [36–38]. This program package is particularly efficient for low-dimensional systems as it employs strictly localized basis sets. Therefore, one does not have to integrate over the empty space between periodic images of the calculated structure in contrast to approaches using plane wave basis sets. In SIESTA the wave functions are written in sets of pseudo-atomic orbitals. For an atom of a given element these functions are calculated from a corresponding pseudopotential. This potential coincides with the real atomic one beyond a certain cutoff radius r_C but is, for $r < r_C$, chosen such that the resulting orbital declines smoothly towards $r = 0$ suppressing the otherwise strong oscillations of the valence wave functions in the vicinity of the core [39, 40]. In order to avoid negligible interaction contributions of orbitals that are situated far apart from each other the pseudo-atomic orbitals are confined by an outer cutoff radius. Due to the strict confinement of the basis functions, SIESTA offers the possibility to perform so-called order-N calculations. These methods are characterized by the computational cost scaling linearly with the number of atoms.
The pseudo-atomic orbitals are expressed as the product of a numerical radial function and a spherical harmonic, which correspond to the shells and the angular momenta, respectively. At the beginning of every calculation the radial functions are derived from the pseudopotentials which have to be provided be the user. This procedure ensures that the basis orbitals and the atomic pseudopotentials used in the simulation are perfectly consistent. One crucial aspect concerns the number of basis orbitals. Obviously, the correct electronic many-body wave functions are described more accurately with an increasing number of basis functions. On the other hand, the computation time and the required memory rise considerably when the basis is extended. The minimal basis consists of one radial component per angular function and is known as single-ζ (or SZ) basis. Adding more radial functions per spherical harmonic results in multiple-ζ basis

sets. Furthermore, SIESTA allows to include higher angular momenta per shell, which are referred to as polarization orbitals. Before starting to study a given system it is necessary to investigate the influence of the basis size on the material properties of interest in order to find a convenient compromise between accuracy and computational cost. This issue is explored comprehensively in Ref. [41].
Several other parameters offer the possibility to further tune the ratio of efficiency and precision. These include the fineness of the real-space integration grid and the k-point sampling of the reciprocal lattice. In order to find a suitable value for a certain parameter it is appropriate to converge the total energy of the system or the maximal atomic force component with respect to this quantity. The Kohn-Sham equations are solved in a self-consistent procedure as described in Sec. 2.1.1 until the density difference between two consecutive loops falls below a tolerance value that can be specified by the user.
In usual calculations, one aims at finding the optimized geometry of a system which yields the minimal total energy. To achieve this task, the conjugate gradient algorithm is implemented in SIESTA [42]. In addition, it is possible to define certain constraints within which the geometric relaxation is to be performed. We make use of this option in our simulations of strained graphene nanoribbons presented in Chap. 6.
The derivation of phonon frequencies and eigenvectors requires knowledge of the force constant matrix. SIESTA uses the method of finite differences to compute the force constants [43, 44]. Within this approach one atom is displaced in a certain direction and the resulting forces on all other atoms are calculated. This procedure is repeated for displacements along all three coordinate axes in positive and negative directions for every atom. Thus, in total, $6N$ displacements are evaluated, with N being the number of atoms. For the calculation of zone center phonons (or molecular vibrations) it is sufficient to consider the atoms of one unit cell. In order to derive the dispersion of phonons one has to include the displacements of all atoms in a sufficiently large super cell.

2.2 Molecular dynamics simulations

2.2.1 Semi-empirical approximations

In a dynamical study of a molecular system the Schrödinger equation must be solved for a large number of different configurations. Doing this by means of *ab initio* methods is only feasible for very small systems due to the otherwise exorbitant computation time. However, the systems typically investigated *via* molecular dynamics simulations comprise large numbers of atoms. Thus, there is a need for more efficient methods than those described in Sec. 2.1. In the field of quantum chemistry a broad variety of approaches have been developed which are based on different *ab initio* theories, but introduce certain approximations employing experimental parameters. These methods are therefore referred to as semi-empirical. The approach used within this work is based on the so-called modified neglect of diatomic overlap (MNDO) [45]. It is derived from the Hartree-Fock theory, *i.e.*, the solutions to the electronic hamiltonian are expressed as Slater determinants. The basic approximation is to neglect overlap integrals of basis

orbitals centered at different atoms [46]. This simplification greatly reduces the number of integrals to be evaluated and thus saves a substantial part of the computational capacity. On the other hand, it is obvious that the electronic interaction is described more roughly than it is by the Hartree-Fock method. In order to compensate for this deficiency, the remaining integrals are parametrized based on atomic and molecular experimental data. The original MNDO approach suggested by Dewar *et al.* has been adjusted in order to overcome certain weaknesses, resulting in the two improved models AM1 and the PM3 [47,48]. Both methods do not show significant differences in efficiency or accuracy for our purpose. In this thesis, we employ the AM1 method as implemented in the simulation package pDynamo [49, 50].

2.2.2 Classical dynamical simulations

The time-dependence of a system can be explored by means of Newton's mechanics. Although neglecting quantum mechanical effects like tunneling, classical simulations still describe the real dynamical behavior properly in many cases. The usual approach is to expand the coordinates of the particles at the times $(t+\Delta t)$ and $(t-\Delta t)$ in Taylor series up to the second order. In this way, coupled recursive formulas can be derived for the developement of $\boldsymbol{r_i}(t)$ and $\boldsymbol{v_i}(t)$ over time, where i denotes the i-th particle. A widely used formulation of these relations is given by the velocity Verlet algorithm which reads [51]

$$\boldsymbol{r_i}(t+\Delta t) = \boldsymbol{r_i}(t) + \Delta t \boldsymbol{v_i}(t) + \frac{\Delta t^2}{2m_i}\boldsymbol{F_i}(t) \tag{2.7}$$

$$\boldsymbol{v_i}(t+\Delta t) = \boldsymbol{v_i}(t) + \frac{\Delta t}{2m_i}\big[\boldsymbol{F_i}(t) + \boldsymbol{F_i}(t+\Delta t)\big]. \tag{2.8}$$

The force on the i-th atom is given by

$$\boldsymbol{F_i} = \frac{\partial}{\partial \boldsymbol{r_i}} V(\boldsymbol{r_1}, ..., \boldsymbol{r_N}), \tag{2.9}$$

where V denotes the potential energy of the N-particle system. At this point, the different methods to approximate the energy of the investigated structure come into play. Since $\boldsymbol{F_i}$ and hence the potential energy have to be computed after every time step Δt, it is practically impossible to use *ab initio* methods for this task. Usually, it is done either *via* molecular mechanical potentials or semi-empirical approaches [49]. We chose the latter option for the simulations presented in this thesis.
At the beginning of a simulation initial velocities must be assigned to the atoms in order to start a dynamical evolution. A suitable method is to choose the velocities such that they comply with the Maxwell-Boltzmann distribution at a desired simulation temperature. During a simulation the system will move along arbitrary directions on the potential energy surface, *i.e.*, kinetic energy will be converted to potential energy and vice versa. Therefore, the temperature corresponding to the atomic velocities will change in general. In order to still maintain a temperature control the velocities are

scaled according to

$$E_{kin} = f\frac{k_B T}{2}, \tag{2.10}$$

where E_{kin} is total kinetic energy of the system with f degrees of freedom. The pDynamo library, which we employ for all simulations in this work, allows the temperature to be scaled either constantly, linearly, or exponentially [49]. The usual procedure is to start a simulation at low temperatures and heat the system up to the desired temperature of interest, for which the actual simulation is then performed isothermal.
One crucial parameter in molecular dynamics simulations is the time step Δt. On the one hand, it is favorable to minimize the computational capacity needed to study a given time period by choosing a large time step. On the other hand, the system is described best using a very small Δt. The value for this parameter should be taken smaller than the time scale of the highest frequency vibrations in the system. It turns out that a reasonable choice for the time step is 1 fs. We used this value in all calculations presented in this work.

3 Carbon picotubes

Parts of this chapter were published in Refs. [52] and [53].

Beginning in 1996, the synthesis of picotubes established a new class of remarkable nanostructures. These highly symmetric, ringlike hydrocarbons are closely related to the smallest possible armchair carbon nanotubes (CNTs). The first picotube to be synthesized was the tetramer molecule [17]. Its structural similarity to a (4,4) CNT was shown to be reflected in the electronic and vibrational properties [54]. Next on the scene were the semitrimer, corresponding to a (3,3) armchair nanotube and Kammermeierphane, a substructure of a (5,5) nanotube [52, 55]. Both compounds reveal strong analogies to the tetramer as well as to nanotubes, as will be discussed below. Another molecule, referred to as tetradehydrodianthracene (TDDA), represents a substructure of the smallest possible armchair tube, the (2,2) CNT and thus completes the series of armchair-like picotubes [17, 56, 57].
The successful synthesis of picotubes represents a crucial step in the field of organic chemistry [58]. Besides their fascinating chemical properties, picotubes are of significant importance with regard to a possible specific synthesis of nanotubes [16]. Up to date methods for the production of CNTs are based on self-organization and therefore yield mixtures of nanotubes of different chiralities and lengths. In many potential electronic applications, nanotubes of a defined chirality would be advantageous. Hence, a controlled, specific production of CNTs is one of the big challenges in nanotube research. Picotubes are possible suitable starting points to achieve this goal [16, 26].
In the following, we first review structural properties of picotubes in Sec. 3.1 before analyzing their most prominent eigenmodes in Sec. 3.2. We further address the dynamic behavior of picotubes inserted into armchair CNTs in analogy to fullerene peapods at different temperatures (Sec. 4) [25].

3.1 Atomic structure

Carbon picotubes can be thought of as short sections from armchair CNTs, but with both ends being opened into several wings. Two examples of the short nanotubes corresponding to picotube molecules are shown in Fig. 3.1. Each of the three smallest picotubes is three hexagons long as indicated by the black section of the (3,3) CNT in Fig. 3.1(a). In contrast, the two halves of Kammermeierphane are arranged with an axial offset of $a_0/2$, where a_0 is the lattice constant of the (5,5) CNT. Thus, the overall length of this molecule is increased by this amount as can be seen in Fig. 3.1(b). In all picotubes, the central hexagons remain linked resulting in a fully conjugated ring. The splitting of the ends leaves anthracene units, *i.e.*, modules of three consecutive carbon

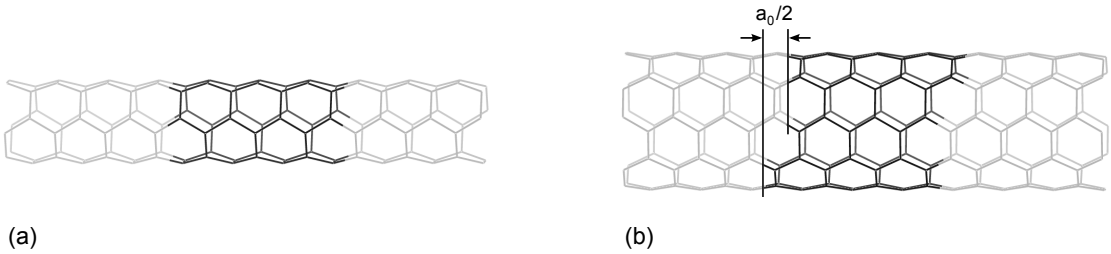

Figure 3.1: (a) Structure of a (3,3) CNT with a section of three carbon hexagons in length being highlighted. (b) Structure of a (5,5) CNT with the black atoms indicating the closed picotube which would correspond to Kammermeierphane.

hexagons, which are arranged in varying regularity depending on the picotube radius. For example, the semitrimer is missing a hexagon at one end and in Kammermeierphane, two dianthracene units are connected by chains which are extended by two additional sp^2 hybridized carbon atoms each. The dangling bonds at the ends are saturated with hydrogen atoms in all picotubes. It should be noted that the described correspondence between the structures of picotubes and nanotubes does by no means represent the way the molecules are produced. Instead, picotubes are designed in a precise bottom-up approach based on ring-expanding reactions of TDDA, the smallest member of the picotube family [17, 55]. In fact, as mentioned above, the synthesis of picotubes is partly motivated by the prospect of gaining CNTs of a defined radius and chirality.
A survey of the picotubes synthesized up to now is presented in Fig. 3.2. The shown structures result from first principles calculations on single molecules with the tetramer data being taken from Ref. [54]. With a diameter of only 2.4 Å, TDDA ($C_{28}H_{16}$) is the smallest possible picotube [57]. Our calculations on the TDDA molecule confirm the experimentally determined radius [57]. This highly strained molecule belongs to the di-

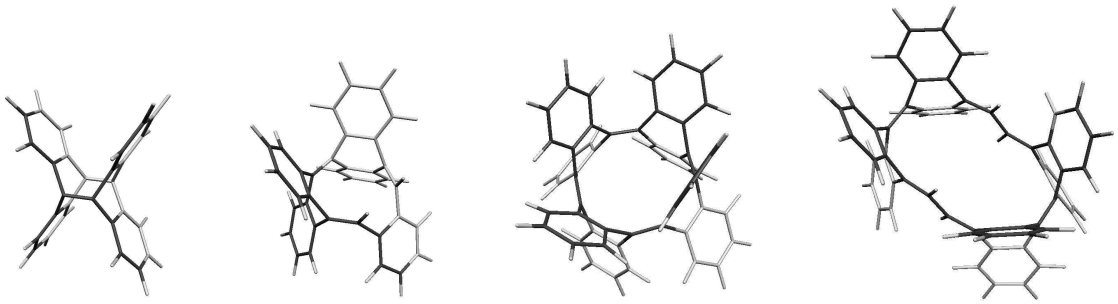

Figure 3.2: Atomic structures of the four smallest carbon picotubes. Foreground (background) carbon-carbon bonds are shown in black (gray) and hydrogen passivations are indicated in light gray.

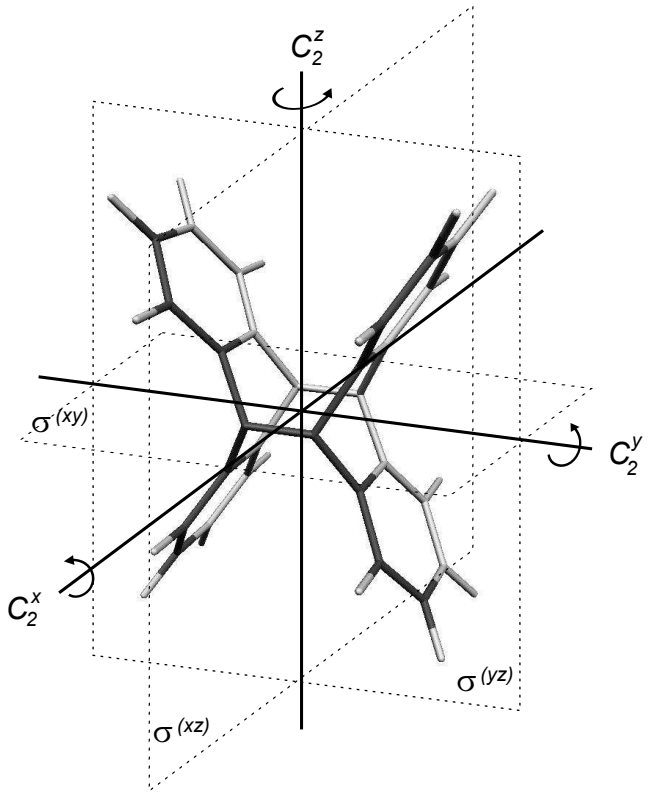

Figure 3.3: Symmetry operations in the TDDA picotube. Solid lines denote 2-fold rotational symmetry and dashed rectangles indicate mirror planes. In addition, the molecule has a center of inversion.

hedral group D_{2h}, with the symmetry operations specified in Fig. 3.3. In the semitrimer ($C_{36}H_{22}$), which is next in size, the symmetry is reduced significantly compared to the other picotubes due to a missing wing (see Fig. 3.2(b)). The resulting group C_{1h}, also referred to as C_s in the literature, contains one mirror plane only [52]. Concerning the size of the semitrimer, our calculations predict a diameter of 4.0 Å, which is close to the diameter of 4.2 Å calculated for a closed (3,3) nanotube [59]. A detailed discussion of the semitrimer structure will be reported elsewhere [60]. The tetramer ($C_{56}H_{32}$) which is shown in Fig. 3.2(c), is another highly symmetric picotube (molecular point group D_{2d}) [54]. In perfect agreement between experiment and theory, the diameter of this molecule was found to be 5.4 Å. This value is again very close to the diameter of the corresponding (4,4) nanotube of 5.5 Å [54]. The structure and symmetry properties of the tetramer are analyzed in detail in Refs. [17, 54]. In contrast to the picotubes described above, the cross-section of Kammermeierphane ($C_{60}H_{36}$) differs considerably from a uniform circle which makes the definition of a diameter difficult (see Fig. 3.2(d)) [55]. Averaging over several atomic distances in the central ring of the molecule, we find a value of 6.5 Å in accordance with the theoretically predicted value for a closed (5,5) nanotube of 6.8 Å [61]. Although being distorted, the molecule clearly represents a subunit of a (5,5) CNT. As visualized in Fig. 3.4, the molecule belongs to the symmetry group C_{2h}. A summary of the structural parameters of all picotubes is given in Tab. 3.1.
All picotubes are available in crystal form. However, neighboring molecules in the solid

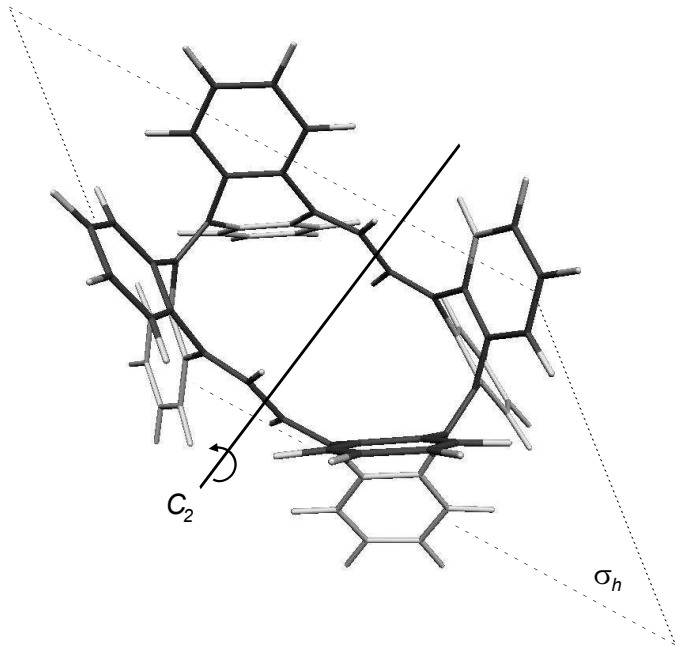

Figure 3.4: The 2-fold rotational symmetry axis and the mirror plane of a Kammermeierphane molecule with a center of inversion symmetry.

have been shown to hardly interact with each other. For tetramer and semitrimer picotubes, an excellent agreement of structural parameters from X-ray scattering of the whole crystal and *ab initio* calculations of isolated molecules has been found [17,54,62]. The same holds for calculated vibrational frequencies of these molecules which are in accordance with results from Raman spectroscopy [52, 54]. As far as TDDA is concerned, our calculations yield again structural parameters matching those determined experimentally very well. These findings clearly indicate that the interaction between picotube molecules in the crystal is weak. Despite the lack of equally comprehensive experimental data about Kammermeierphane, we assume that our computational results about this molecule approximate the properties of the associated picotube crystal similarly well.

3.2 Vibrational properties

In the following, we concentrate on the vibrational eigenmodes of the series of picotubes described above. Raman measurements performed on semitrimer and tetramer picotubes reveal strong similarities among each other as well as to the vibrational spectrum of carbon nanotubes [52, 54]. By means of polarized Raman spectroscopy combined with *ab initio* simulations, a well-defined assignment of eigenvectors to measured Raman peaks was found allowing a direct comparison of semitrimer and tetramer eigenmodes [53, 54]. In this context, we analyze the DFT-derived vibrations of TDDA and Kammermeierphane. As will be discussed below, the behavior of the most characteristic eigenmodes, the radial breathing mode (Sec. 3.2.1) and the high-energy modes (Sec. 3.2.2), reconfirm the analogies in the spectra of picotubes and CNTs.

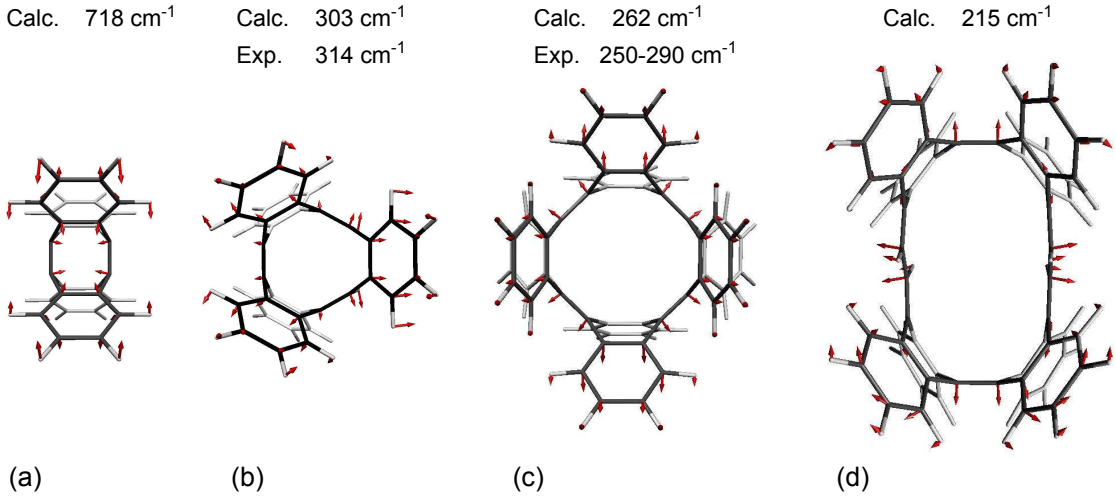

Figure 3.5: Eigenvectors and frequencies of the RBM in different picotubes. For clarity, foreground (background) carbon-carbon bonds are indicated black (gray), and the atomic displacements of the background atoms are omitted.

3.2.1 Radial breathing mode

For semitrimer and tetramer picotubes, radial breathing modes (RBMs) have been identified in *ab initio* calculations. Like in CNTs, these vibrations show an in-phase radial displacement of all carbon atoms. Our calculations on TDDA and Kammermeierphane predict breathing-like modes in these compounds, too. Figure 3.5 shows the RBM eigenvectors derived for the four different picotubes together with their calculated frequencies and the experimentally determined frequencies in semitrimer and tetramer crystals [52, 54]. The displacement patterns of all RBMs are fully symmetric just as found for nanotubes. Thus, it is expected that the mode gives rise to a strong Raman signal, which has indeed been found for semitrimer and tetramer crystals. Please note that the semitrimer data shown in Fig. 3.5 is from DFT calculations in the local density approximation (LDA) in contrast to the results shown in Ref. [52] which have been derived by means of the B3LYP functional. The eigenfrequencies derived *via* LDA slightly differ from those given in Ref. [52], but show a better overall agreement with Raman measurements.

Although the molecular structure of picotubes deviates considerably from that of closed nanotubes, the RBMs exhibit atomic displacements which are predominantly in radial direction and in phase. The strongest discrepancy from a breathing-like motion occurs in the eight wings of Kammermeierphane (see Fig. 3.5(d)). Due to the elongated cross section of the molecule, a radial direction is not clearly defined. Furthermore, Kammermeierphane has two centers of mass linked by two comparably long carbon chains. In this configuration, a breathing-like motion of the central ring leads to a tangential bending of the wings towards the two connecting carbon chains. Nevertheless, the overall breathing-like character of the vibration is evident.

Table 3.1: Characteristic structural and vibrational parameters of carbon picotubes. The radii and RBM frequencies of the picotubes result from first principles calculations [54]. The RBM frequencies of the corresponding nanotubes are derived using the frequency-diameter dependence found by Telg *et al.* and calculated nanotube diameters [54, 59, 61, 63].

	Chem. formula	Symmetry	Radius (Å)	ω_{RBM} (cm^{-1})	$\omega_{RBM}^{nanotube}$ (cm^{-1})
TDDA	$C_{28}H_{16}$	D_{2h}	2.4	718	
semitrimer	$C_{36}H_{22}$	C_{1h}	4.0	303	531
tetramer	$C_{56}H_{32}$	D_{2d}	5.4	262	408
Kammermeierphane	$C_{60}H_{36}$	C_{2h}	6.5	215	334

In the spectroscopic characterization of CNTs, the RBM is of central importance as it offers a fingerprint of the specific type of the tube [13, 64, 65]. This is particularly expressed by the direct relation between the energy of this mode and the nanotube radius. The RBM frequency of a nanotube increases with decreasing tube diameter, since smaller tubes are more strained. In principle, we expect the same effect in picotubes. The splitting of the tube wall into separate wings in picotubes leads to a reduced effective curvature and hence a lower strain in picotubes compared to CNTs. Therefore, we expect the RBMs at lower energies in picotubes than in nanotubes in accordance with the observations made on semitrimer and tetramer picotubes [52, 54]. As shown in Tab. 3.1, this assumption is confirmed by comparing the RBM frequencies of Kammermeierphane and a (5,5) CNT. The theoretically determined RBM frequencies of the investigated picotubes versus their diameter are plotted in Fig. 3.6. The red fit curve was obtained using the frequency-diameter relation of carbon nanotubes $\omega_{RBM} = C_1/d + C_2$ [13].

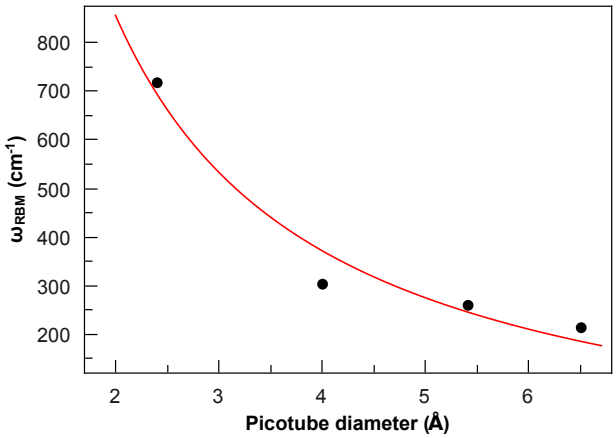

Figure 3.6: Calculated RBM frequencies of carbon picotubes as a function of the diameter. The red curve represents a $1/d$-fit.

Obviously, the picotube data available up to now roughly satisfies this relation using the parameters $C_1 = 1938\,\mathrm{cm}^{-1}$ nm and $C_2 = -113\,\mathrm{cm}^{-1}$. The RBM frequency of the semitrimer is lower than according to the d^{-1} - dependence. This possibly originates from the fact that the structure of the molecule is further relaxed due to one missing wing. A full trimer, which has not been synthesized yet, most likely yields a higher RBM frequency. We expect the same effect to occur in the case of Kammermeierphane as this molecule consists of four anthracene units in contrast to a hypothetical complete (5,5) picotube.
Another issue concerns the value derived for C_2 which would imply negative RBM frequencies at large picotube diameters. The strongly negative value stated above can be partially attributed to the lowered frequencies of the Semitrimer and Kammermeierphane picotubes compared to those expected for full (3,3) and (5,5) picotube molecules. Furthermore, it should be noted that the RBMs of very small nanotubes show deviations from an ideal d^{-1} - dependence [66]. Possibly, a similar effect in picotubes might affect our results. In order to clarify this issue, larger picotubes will have to be considered which have not been synthesized up to now.

3.2.2 High-energy modes

The Raman spectra of semitrimer and tetramer picotubes are dominated by high-energy bands at about $1600\,\mathrm{cm}^{-1}$, which is typical for curved sp^2 carbon compounds [52, 54]. In case of armchair CNTs, this band contains vibrations along and perpendicular to the tube axis, referred to as longitudinal (LO) and transversal (TO) optical modes, respectively [13]. Calculations on picotube molecules predict eigenmodes with analogous displacement patterns. Since picotubes are not subject to translational symmetry in contrast to CNTs, the molecules show plenty of LO- and TO-like modes. This is illustrated by the displacement patterns of high-energy modes of different picotubes presented in Fig. 3.7. For example, the longitudinal semitrimer mode shown on the right side of Fig. 3.7(c) exhibits an opposite-phase motion of the atoms in the lower and upper hexagons. The direct counterpart of this mode in the corresponding (3,3) CNT is forbidden by symmetry at the Γ point as it would mean different atomic displacements in neighboring unit cells of the tube.
The main contributions to the high-energy Raman band of tetramer picotubes can be ascribed to totally symmetric modes [54]. These are transversal vibrations, since LO modes are antisymmetric with respect to the mirror planes of the molecule. Accordingly, the longitudinal mode shown in Fig. 3.7(d) can not be assigned to a measured Raman peak. The same situation applies to TDDA, where only TO modes are totally symmetric. From group theory, all eigenmodes which are invariant under inversion are expected to be Raman active (see App.) [67]. Apart from the fully symmetric A_g modes, this includes eigenvectors transforming according to the representations B_{1g}, B_{2g}, and B_{3g}, each of which is antisymmetric with respect to two out of the three 2-fold rotations and two out of the three mirror planes (see Fig. 3.3). However, totally symmetric vibrations generally are expected to exhibit stronger Raman intensities than antisymmetric ones in agreement with the findings on semitrimer and tetramer crystals [68]. Therefore,

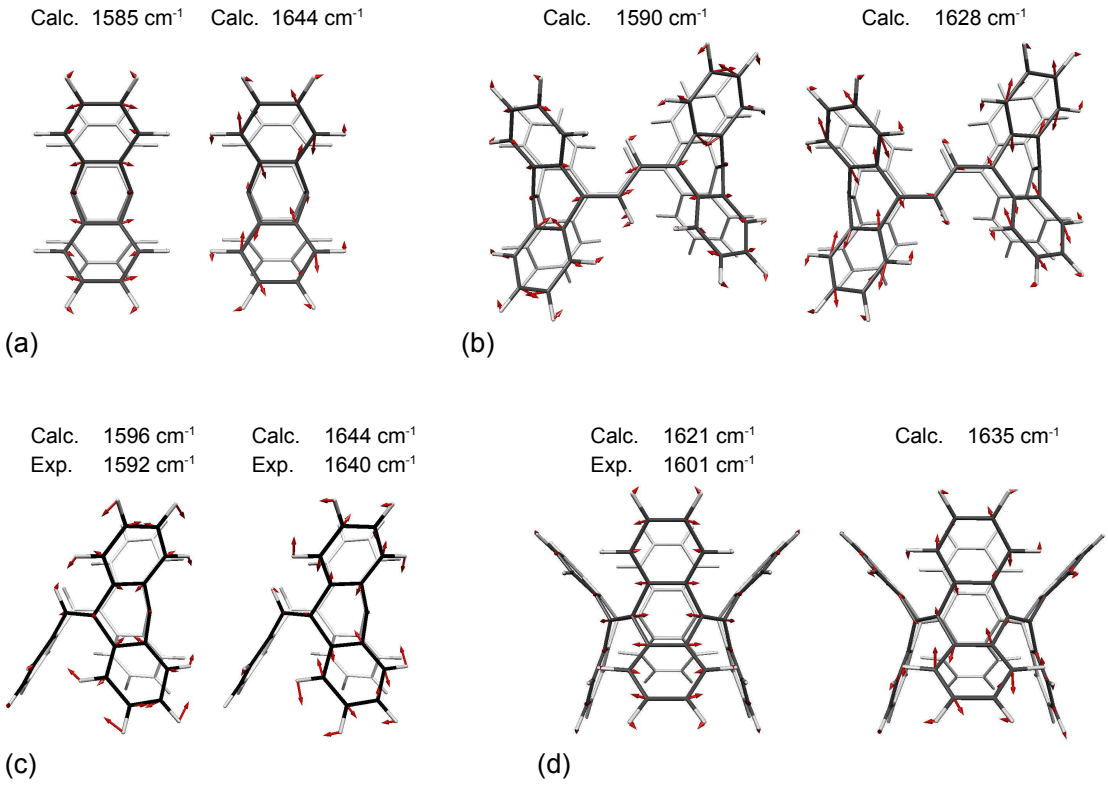

Figure 3.7: Eigenvectors and calculated frequencies of selected high-energy vibrations of (a) TDDA, (b) Kammermeierphane, (c) semitrimer, and (d) tetramer picotubes. For each molecule, we show a longitudinal (left) and a transversal vibration (right). Experimental frequencies are assigned to the two semitrimer modes and the transversal tetramer mode (see left pattern in (d)) [54]. For clarity, background atoms are shown in gray and displacement arrows in the background are omitted.

we assume that the high-energy Raman signal of TDDA picotubes can be attributed to TO modes. Our calculations predict two such modes at $1609\,\mathrm{cm}^{-1}$ and $1585\,\mathrm{cm}^{-1}$, the latter of which is shown in Fig. 3.7(a). Thus, Raman experiments on TDDA most probably exhibit a narrow, clearly structured high-energy band similar to the tetramer spectrum. The behavior described above is equivalent to that of armchair CNTs, for which the axial E_{1g} high-energy phonons are not expected to yield considerable Raman intensity [13].

In principle, the above considerations can be transferred to the semitrimer molecule. Nonetheless, we find totally symmetric A' vibrations with pronounced LO-like displacement patterns in both complete anthracene units of the semitrimer. In the single carbon hexagon forming the third - partial - anthracene block, neighboring atoms do not move in opposite phase, but in phase, which leaves the pattern symmetric with respect to the mirror plane σ_h, the only non-trivial symmetry element of the semitrimer point group. The eigenvector shown in Fig. 3.7(c) is an example for an A' longitudinal mode of the

semitrimer. Although not all of the - much lighter - hydrogen atoms, which terminate the dangling carbon bonds, follow the axial motion of the carbon atoms, the LO character of the vibration is evident. We conclude that longitudinal as well as transversal modes contribute to the semitrimer high-energy band giving rise to the extended Raman band in this region compared to tetramer picotubes [52–54]. Furthermore, the number of fully symmetric modes is higher for semitrimers than for all other picotubes due to the low symmetry of the molecule [52].
Similar to the semitrimer case, the structure of Kammermeierphane picotubes allows both LO and TO eigenvectors with the full symmetry of the molecular point group. This is a consequence of no anthracene unit being crossed lengthwise by a mirror plane as can be seen in Fig. 3.4. Like the TDDA picotube, Kammermeierphane has an inversion center, which limits Raman activity to the modes that are invariant under this symmetry transformation as described in the appendix. However, it is expected that the B_g modes, which are antisymmetric with respect to the rotation C_2 and the mirror plane σ_h, yield lower Raman intensity than A_g modes [67]. Our simulations show a total of five fully symmetric modes in the high-energy region, two of which exhibit longitudinal displacements and three have transversal character. One example of each group is presented in Fig. 3.7(b). Thus, our results suggest that the high-energy Raman band of Kammermeierphane is similarly broadened as found for semitrimer picotubes.
All picotubes have in common that the LO vibrations are found at higher frequencies than the TO modes. This is in contrast to the corresponding armchair nanotubes, which exhibit softened LO phonon frequencies due to a Kohn anomaly effect: The lattice distortion of the LO phonon leads to a band-gap opening in these otherwise metallic CNTs, which compensates part of the energy needed to distort the tube [13, 69, 70]. In nanotubes which are not subject to this mechanism, *i.e.*, in semiconducting tubes, the LO mode frequency exceeds that of the TO mode [13]. A similar effect for molecules, which could damp the LO mode frequencies of picotubes in analogy to those of armchair CNTs, is not known.

3.3 Summary

We performed a comparative *ab initio* study of the structures and vibrations of four consecutive carbon picotubes. These ring-shaped hydrocarbons closely resemble narrow armchair nanotubes. Therefore, picotubes are considered to be possible starting points for a specific synthesis of carbon nanotubes. The structural regularity and symmetry differ considerably among the different picotube types, which is reflected in the molecular vibrations as well. The vibrations of picotube molecules and nanotubes show similar characteristics. Whereas the high-energy band of two picotube species is expected to be dominated by transversal optical modes analogous to armchair nanotubes, the lower symmetry of the two other picotubes allows both totally symmetric longitudinal and transversal optical vibrations. This is in accordance with previous Raman experiments on semitrimer and tetramer picotubes. Furthermore, our calculations of picotubes exhibit radial breathing modes and thus counterparts to the well-known fingerprint modes

of carbon nanotubes. The breathing-mode frequencies of picotubes roughly satisfy a d^{-1} - dependence in accordance with the relation in carbon nanotubes.

4 Molecular dynamics of picotube peapods

Parts of this chapter were published in Ref. [71].

An intriguing question about carbon picotubes concerns the possibility to obtain closed nanotubes of a well-defined chirality from these molecules. In a first step, this would require the transformation of the picotube structures presented above into short nanotube sections with closed ends. These building blocks might subsequently serve as starting points for the formation of longer tubes under appropriate conditions [16]. Schaman *et al.* suggest an approach to configurate picotubes to a tubular structure by means of the interaction of picotubes with CNTs [26]. They report about Raman experiments which point to a successful formation of closed picotubes. Furthermore, the authors present two interesting theoretical results: First, according to their *ab initio* calculations, the tubular configuration of the tetramer is favorable compared to the one with separate wings at the ends. In addition, they show an energy gain for the encapsulation of picotubes in certain types of CNTs. These findings motivate a further investigation of how picotubes behave in the presence of nanotubes and, in particular, *inside* nanotubes. We address this question by studying the dynamic behavior of tetramer molecules inserted into armchair nanotubes in analogy to fullerene peapods [25, 72]. This system is examined by means of molecular dynamics simulations under varying thermal conditions. In the following, we first describe the simulated system and demonstrate the suitability of the applied semi-empirical model (Sec. 4.1). In Sec. 4.2, we show that the dynamics of the picotube-nanotube system can be classified into oscillations, axial transport, and structural reconfiguration of the picotubes.

4.1 Setup of the simulation

4.1.1 Composition of the investigated system

All picotubes presented in Chap. 3 are prospective starting points for the synthesis of the corresponding closed nanotubes. However, the tetramer seems to be the most appropriate candidate. Semitrimer and Kammermeierphane picotubes are of a less regular structure than the tetramer molecule, which impedes the formation of nanotubes due to missing sections in the potential tube wall. TDDA, the second highly symmetric and regular picotube apart from the tetramer, corresponds to the (2,2) CNT, which is considered hypothetical as it would be highly strained. Thus, we choose tetramer picotubes for our simulations.
The choice of the surrounding tube has to fulfill two requirements: First, the tube diam-

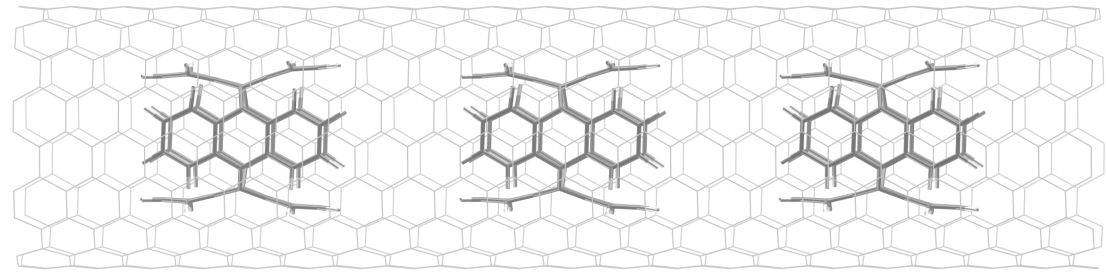

(a)

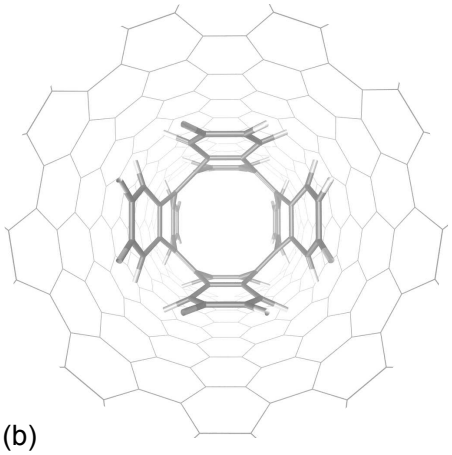

(b)

Figure 4.1: (a) Initial configuration of three consecutive tetramer molecules encapsulated coaxially in a (9,9) CNT. (b) Axial view of the position of a tetramer molecule oriented coaxially inside the (9,9) nanotube.

eter should be large enough to ensure that no bonds form between the hydrogen atoms of the tetramer and the tube wall. On the other hand, the number of atoms, *e.g.*, the computation time, is minimized by taking the smallest possible tube. Concentrating on armchair tubes, the (9,9) nanotube with a diameter of 1.22 nm turns out to be a suitable candidate. In this type of nanotube, the most likely orientation of a tetramer molecules is coaxial as shown in Fig. 4.1. This configuration possibly facilitates a transformation of the picotubes towards short closed tubes.

As mentioned above, the encapsulation of a tetramer into a (19,0) tube, which has a larger diameter of 1.49 nm compared to the (9,9) tube, results in an energy gain [26]. In contrast, inserting a tetramer into a (9,9) nanotube requires an energy input of 15 eV. Nevertheless we consider the narrower (9,9) nanotube a better model case for two reasons: First, the interaction between the tube and the tetramer molecules, which is the main subject to the present investigation, is expected to play a greater role in a narrower tube. Furthermore, the inter-wall distance of 3.35 Å in a (4,4)@(9,9) double wall nanotube that might potentially evolve from the tetramer-nanotube system, comes very close to the values predicted and found for actual double wall tubes [73, 74]. Therefore, we expect the possible formation of an inner (4,4) nanotube from the tetramer molecules to be favored by this choice for the outer tube.

Besides the picotube-nanotube interactions, mutual influence of different tetramer molecules might have an impact on the dynamic behavior. In order to cover interactions

Table 4.1: Structural parameters of the tetramer molecule as calculated within the AM1 approximation compared to reference values from *ab initio* simulations and x-ray diffraction [54].

		AM1	DFT	x-ray
Diameter (Å)		5.4	5.4	5.4
C-C bond lengths (Å)	1	1.35	1.37	1.36
	$2i$	1.48	1.49	1.51
	$2o$	1.47	1.48	1.49
	$3i$	1.43	1.43	1.42
	$3o$	1.42	1.42	1.41
	$4i$	1.39	1.40	1.39
	$4o$	1.39	1.40	1.39
	$5i$	1.40	1.40	1.39
	$5o$	1.40	1.40	1.39
	$6i$	1.39	1.40	1.39
	$6o$	1.39	1.40	1.39
C-H bond length (Å)		1.10	1.11	0.99
C-C-C angles (°)	$2i-2o$	108	109	108
	$1-2i$	126	126	126
	$1-2o$	126	125	126
Wing angles (°)	θ	48	51	51
	ϕ	71	73	70

between the picotubes we comprise three consecutively arranged tetramers in our studies. The resulting input configuration for the dynamical simulations is shown in Fig. 4.1.

4.1.2 Suitability of the computational approach

The configuration described above contains 1020 atoms in total. Given the large number of time steps evaluated in molecular dynamics simulations, the use of *ab initio* methods for such a large system would require disproportionately high computational resources. Instead, we employ the semi-empirical AM1 approach introduced in Sec. 2.2.1, which is widely used in molecular dynamics studies involving nanotubes [47, 75–77]. In the following we demonstrate the accuracy of this method with respect to the particular composition of picotubes.

We first simulate an isolated tetramer and compare the results to previous reference work. Figure 4.2 shows the AM1-relaxed structure of the tetramer. The notation of the different bonds is largely adopted from Ref. [54]. As shown in Tab. 4.1 the bond lengths and angles found by means of the AM1 model are in excellent agreement with the results

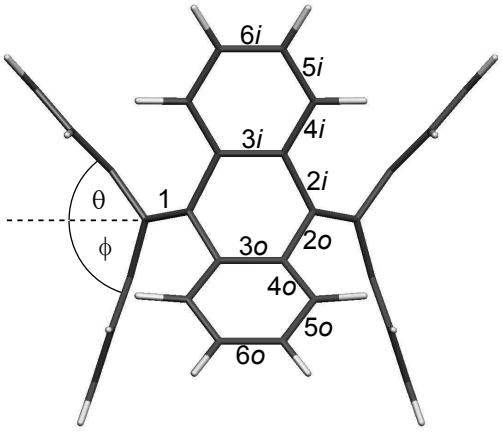

Figure 4.2: The tetramer picotube as seen from the side. We adopt the bond labeling introduced in Ref. [54], according to which the indices i and o denote bonds in the wings bending inward and outward, respectively.

of DFT calculations and x-ray scattering experiments. The configuration of the tetramer shown here, which has D_{2d} symmetry, represents the global minimum of the potential energy surface. Actually, the molecule has been shown to oscillate rapidly between two equivalent D_{2d} states by interchanging in- and outward bending benzene wings [17]. This leads to a time-averaged intermediate state with D_{4h} symmetry, which corresponds to a local energy maximum. Our calculations show the energy of this metastable configuration to be 266 meV higher than that of the two D_{2d} structures in accordance with the DFT-derived value and a prior AM1 study [17, 54]. These results indicate that tetramer picotubes are described accurately within our approach. In addition, our calculations confirm the energy gain from inserting a tetramer into a (19,0) nanotube reported earlier [26]. We find the encapsulation in this tube to be favorable by 1.44 eV in agreement with Schaman *et al.* who found an energy difference of 1.2 eV.

4.2 Temperature-dependent dynamics

To develop a comprehensive picture of the dynamical behavior of tetramer molecules inside (9,9) nanotubes, we perform simulations at various temperatures ranging from 100 K up to 3000 K. We observe three independent effects in different temperature ranges. At low temperatures the picotubes perform periodic motions inside the nanotube (Sec. 4.2.1). Depending on the particular simulation temperature we find axial oscillations, rotations about certain axes perpendicular to the nanotube wall, and superpositions of different modes. Above 800 K the tetramers move collectively along the nanotube axis (Sec. 4.2.2). Further investigations reveal that in the case of individual picotubes inserted into nanotubes, this transport effect occurs already at much lower temperatures. While previous investigations on transport in carbon nanotubes are based on pressure gradients, external electric fields, or thermophoretic forces, our simulations yield molecular transport as a consequence of a homogeneous heating of the whole system [78–80]. Another remarkable result is found for temperatures above 2500 K (Sec. 4.2.3). We observe a partial dehydrogenation of the tetramer molecules as well as the formation of new bonds. Eventually, this may lead to the transformation of the open

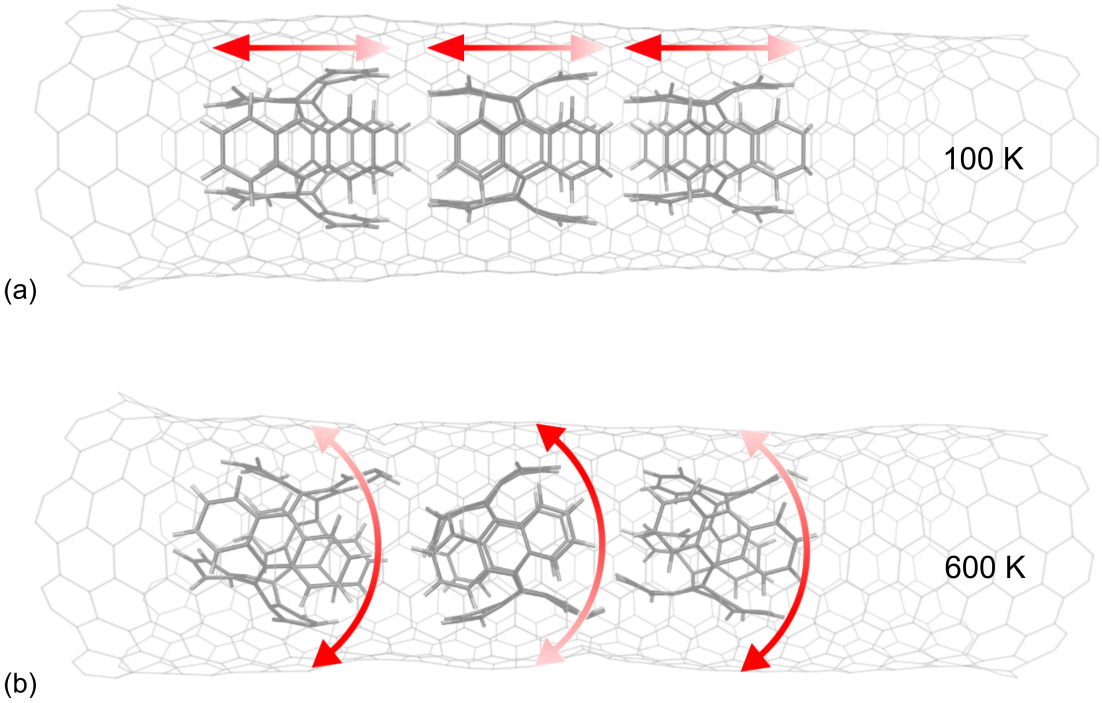

Figure 4.3: Motional patterns of the tetramers inside the nanotube at low temperatures. Bright ends of the red arrows denote in-phase states of the single molecular oscillations.

picotubes to a closed tubular configuration as suggested by Schaman *et al.* [26].

4.2.1 Low temperature oscillations

Two different periodic motions of the picotubes are shown in Fig. 4.3. When cooled down to 100 K the tetramers perform an in-phase oscillation along the axis of the surrounding nanotube (see Fig. 4.3(a)). The frequency of this oscillation compares to an energy of about 2.2 meV and thus a factor of ten less than the energy of the radial breathing modes of the smallest pico- and nanotubes [53,54]. Figure 4.3(b) shows an opposite phase rotation of neighboring tetramers around axes perpendicular to the nanotube axis. The image shown here stems from a simulation at 600 K, but the same rotational pattern is also found at lower temperatures. At 400 K, one tetramer even performs a rotation by 180° about an axis perpendicular to the nanotube. In all simulated cases, the oscillation presented here is superimposed by axial modes of the molecules resulting in complicated motional patterns which are less regular than the one shown in Fig. 4.3(a). Therefore, it is not possible to determine a frequency of the rotational mode.
Superpositions of different oscillations occur throughout most of the lower thermal range. In general, the out-of-phase motion of all picotubes with different frequencies thereby leads to a complex vibrational pattern. In cases of nonuniform axial motions we observe elastic collisions of the molecules. Subsequently, tetramers which do not collide again

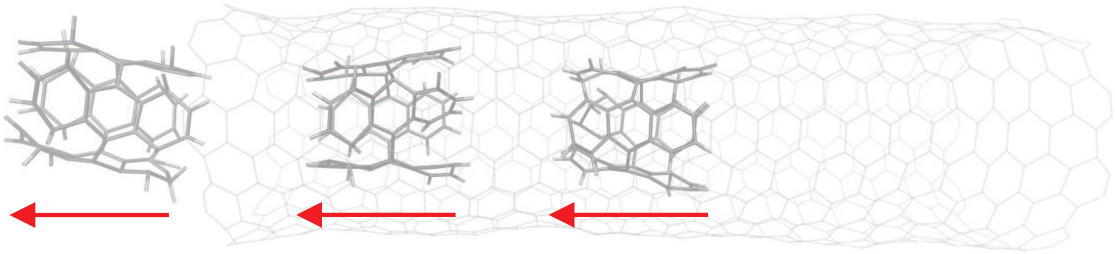

Figure 4.4: Transport of the picotubes through the nanotube at a simulated temperature of 2000 K. All tetramer molecules move to one end of the tube simultaneously.

move continuously through the nanotube. This effect will be described in more detail in Sec. 4.2.2. One possible additional degree of freedom of the tetramer molecules is given by rotary oscillations about the nanotube axis. However, we do not observe such a vibration in any simulation.

4.2.2 Molecular transport

A qualitatively different effect compared to the oscillations described above is found at higher temperatures. As shown in Fig. 4.4 at a temperature of 2000 K the three picotubes move towards one end of the nanotube and do not oscillate against each other. The simultaneous motion of all molecules sets in at about 800 K. However, at this temperature the motion of the molecules is not perfectly collective but the rearmost picotube follows the first two at a lower velocity. With increasing temperature all three tetramers move synchronously as can be seen in the example shown in Fig. 4.4. The molecular transport also occurs if a single tetramer is encapsulated in the nanotube. In this case, we observe a continuous motion already at temperatures as low as 50 K. Apparently, the interaction among different picotubes leads to a higher thermal energy being required to enable a collective motion of the whole picotube ensemble. We choose the simplified case of an individual tetramer to further study the conditions of the picotube transport. In doing so, we can reduce the length of the surrounding nanotube compared to the configuration shown in Fig. 4.4 and thus save computational capacity.
The higher total potential energy of the system with the tetramer situated inside the nanotube suggests that the tetramer follows an energy gradient towards the tube end. In order to clarify this issue we performed simulations with a tetramer placed at different positions along the nanotube axis. These calculations show that the direction the picotube moves in does clearly not depend on the distance to the nearest end of the nanotube. When placed near one end of the nanotube, the picotube in some cases still moves all the way to the opposite end before escaping the nanotube. This result strongly indicates that effects induced by the tube ends are irrelevant.
Obviously the motion is driven by interactions of the picotubes with the nanotube wall. We therefore consider the symmetry of the entire system which depends on the initial position and orientation of the tetramer in the nanotube. The two parameters that

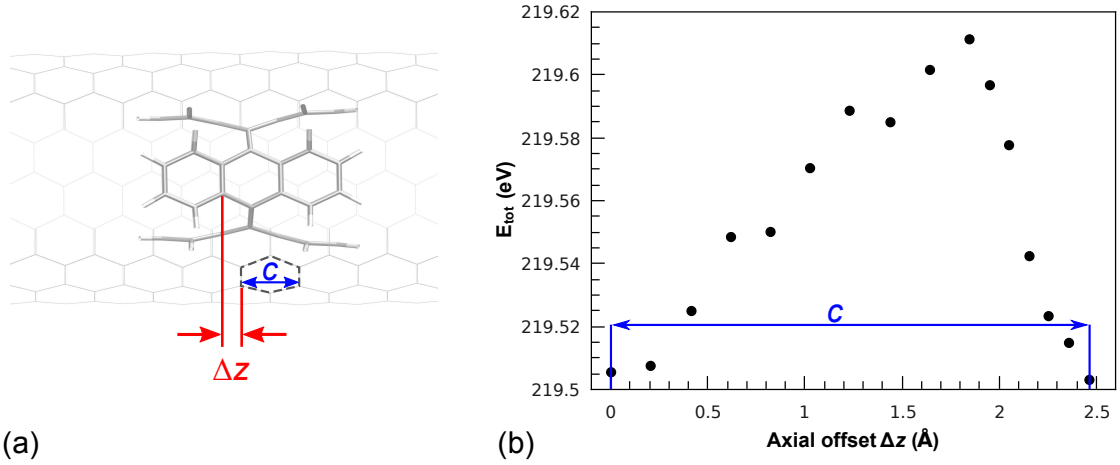

Figure 4.5: (a) Relative axial position of a tetramer picotube inside a (9,9) carbon nanotube. Δz denotes the offset of the tetramer with respect to a hexagon in the nanotube wall and c is the lattice constant of the tube. (b) Total energy of the complete system depending on the relative axial offset as defined in (a).

determine the relative configuration of both compounds are the axial position Δz of the tetramer with respect to the unit cell of the nanotube (see Fig. 4.5(a)) and the angular orientation $\Delta\alpha$ (see Fig. 4.6(a)). We find the potential energy of the system to depend on the axial offset as shown in Fig. 4.5(b). A picotube moving along the nanotube axis undergoes a varying potential and thus encounters small local energy gradients. The height of the energy barrier along the unit cell of the nanotube is 110 meV in total and 0.27 meV/atom. Notably, this value is very close to the translational potential barrier of 0.23 eV/atom derived for a double wall carbon nanotube composed by a (5,5) and a (10,10) CNT [81]. The interlayer distance of the latter system is comparable to the distance between the picotube 'wall' and the surrounding (9,9) nanotube. The energy barrier stated above impedes an axial translation of the picotube only close to absolute zero. Accordingly, our simulations exhibit a motion of individual tetramer molecules through the nanotube down to a temperature of 50 K. Most probably, molecular transport will be observable even at lower temperatures. However, the mean velocity of the picotubes strongly decreases when cooling down the system. Thus, detecting a translation at lower temperatures requires the simulation of a longer time span, which limits the technical feasibility of such a study. The total energy as a function of the angular orientation is shown in Fig. 4.6(b). Due to the 9-fold symmetry axis of the nanotube, the potential exhibits a periodicity of 40°. The energy varies in a margin of about 100 meV in correspondence to the axial barrier height.
The picotubes move in randomly distributed directions independent of the temperature. A possible influence of the local energy gradients in the phase space spanned by Δz and $\Delta\alpha$ on the direction of motion is examined by varying the initial position and orientation of the tetramer and starting a dynamical simulation in each case. Our findings clearly

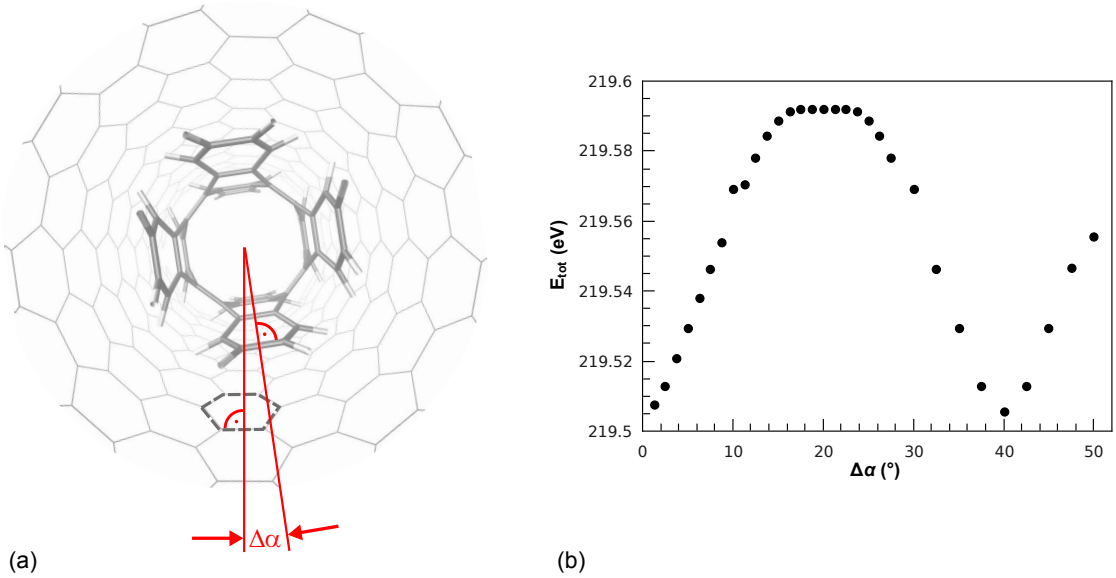

Figure 4.6: (a) Relative angular offset between a tetramer picotube and the surrounding (9,9) nanotube. (b) Total energy of the system depending on the relative orientation $\Delta\alpha$ as defined in (a).

show that there is no connection between the direction of the axial momentum obtained by the molecule and the gradient of the potential at the initial position.
While the velocity of the picotubes approaches zero at low temperatures, we find values of the order of 10^3 m/s for 1000 K. Simulations at several temperature levels up to 2500 K yield an increase of the mean tetramer velocity. From 2500 K on, the picotubes again move slower as the thermal energy is partially taken up by additional reconfiguration effects in the molecules as described in the following Section.

4.2.3 Chemical modifications

Another remarkable result is found for very high temperatures. Above 2500 K the thermal energy allows the breaking of carbon-hydrogen bonds in the picotubes. The dehy-

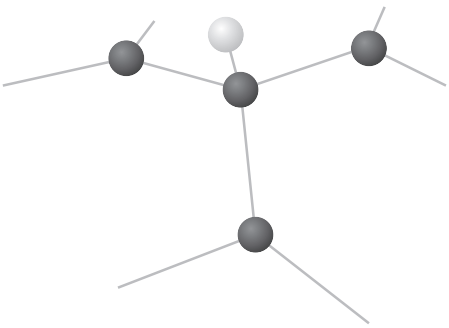

Figure 4.7: Schematic view of a hydrogen atom (light gray) bound radially to a closed tubular wall of carbon atoms (black).

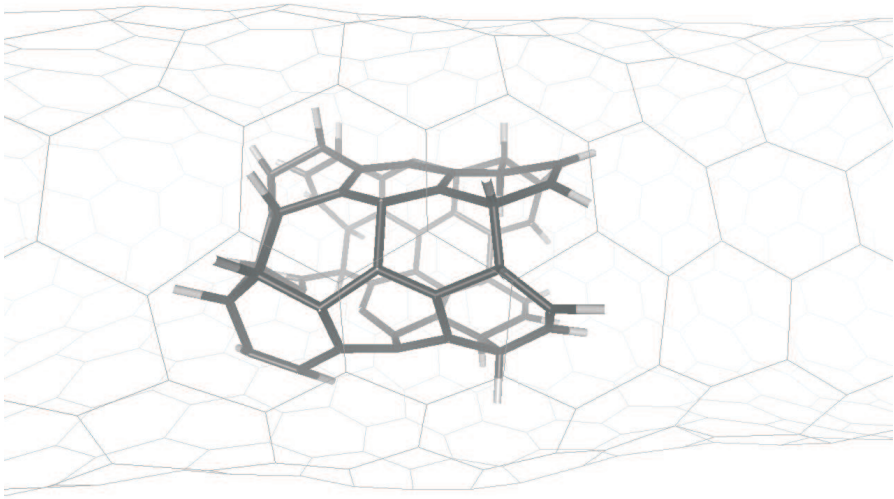

Figure 4.8: Close-up view of a tetramer molecule during a simulation at a temperature of 2500 K. Obviously a structural reorganization takes place resulting in an almost closed configuration, *e.g.*, a very short (4,4) nanotube.

drogenated outer carbon atoms at the wings of the tetramer tend to form new bonds, which leads to a closing of the tetramer wings to a tubular configuration. However, our simulations show the removal of only a few hydrogen atoms of the picotubes. Mostly sp^3-like configurations form as a result of a hydrogen atom being attached to the outside of a closed tubular section of the tetramer (see Fig. 4.7). The resulting partially closed picotube structure with radially oriented C-H bonds is shown in Fig. 4.8. Those hydrogen atoms which are removed from the picotube join and form H_2 molecules inside the nanotube. Furthermore, at 3000 K we observe the dissociation of entire C_2H_2 groups of the tetramer molecules. The latter effect also results in a tubular structure, although a shorter one. Anyhow, a temperature of 3000 K seems to be too high to achieve a preparation of a closed (4,4) tube as the tetramer structure starts to become unstable. This will presumably promote the formation of defects in the produced tube. The surrounding (9,9) nanotube remains unaffected of any chemical modification in all of our simulations.

A transformation of the open tetramer to a closed picotube structure is consequential as this process has been shown to reduce the potential energy [26]. Nevertheless, it is an intriguing result which at longer simulation times might lead to a fully dehydrogenated closed configuration. In fact, it is the first step to a selective formation of a (4,4) nanotube.

4.3 Summary

We presented a molecular dynamical study on the behavior of tetramer picotubes aligned inside a (9,9) nanotube. Our investigations in this field of interacting pico- and nanotubes yield several interesting results. At low temperatures we observe rotations and axial vibrations of the tetramers inside the nanotube. Furthermore, a molecular transport occurs at arbitrary temperatures in the case of individual picotubes and from 800 K on if a group of interacting picotubes is considered. Finally, we find a structural transformation of the tetramer molecules inside the nanotube at higher temperatures. At 2500 K the thermal energy causes the breaking of C-H bonds and the formation of new bonds. Different structural transformations of the tetramer molecules result in short, tubular structures. This is a promising result on the way to a possible chirality-selective preparation method of carbon nanotubes.

5 Basic properties of graphene nanoribbons

Parts of this chapter were published in Refs. [82, 83].

Graphene has drawn extensive research interest since its discovery in 2004 [5]. This two-dimensional carbon allotrope exhibits a broad range of fascinating characteristics. The planar, hexagonal configuration of carbon atoms represents the thinnest possible membrane which at the same time proofs to be extraordinarily stable [8]. However, great potential of graphene is also to be found in its remarkable electronic properties. Graphene is a semimetal, *i.e.*, a zero-band-gap semiconductor. Its Fermi surface exists only at the corners of the Brillouin zone, the six K points. The bands formed by the π orbitals of the sp^2 hybridized carbon atoms show a locally linear dispersion near the Fermi level. This unusual band structure allows a formal treatment of the electrons as quasi-relativistic Dirac fermions, with a Fermi velocity of $v_F \approx 1 \cdot 10^6\,\mathrm{m/s}$ [5, 84–86]. The exceptional electronic configuration of graphene is also reflected in the observation of the quantum hall effect at room temperature [87]. These findings have triggered tremendous efforts towards applications and the first graphene transistors have shown very high charge mobilities of up to $20000\,\mathrm{cm^2/(V{\cdot}s)}$ [12]. Despite its striking electronic features, the gap-less band structure of graphene impedes a direct use in many potential nanoelectronic devices. A possible way to overcome this obstacle is to design narrow stripes of a graphene sheet, which opens a gap due to the lateral confinement of the electronic wave function [18, 19, 88]. These so-called graphene nanoribbons (GNRs) are therefore considered promising building blocks in future nanoelectronic circuits [89–91]. In the following, we will review the fundamental properties of intrinsic GNRs, starting with geometrical aspects in Sec. 5.1. Subsequently we address how different edge configurations and widths affect the electronic and vibrational properties of GNRs (see Secs. 5.2 and 5.3).

5.1 Edge types and classification

There are unlimited possibilities of how to cut a ribbon out of a graphene sheet, giving infinite possible edge geometries. However, recent reports on imaging of graphene by means of high-resolution transmission electron microscopy suggest that edges favorably form along the crystal directions [92, 93]. These so-called armchair and zigzag directions of the hexagonal graphene lattice are illustrated in Fig. 5.1. As edges along these lines are expected to be most stable, the majority of the research work on GNRs concentrates on ribbons cut in these directions, *i.e.*, armchair GNRs (AGNRs) and zigzag

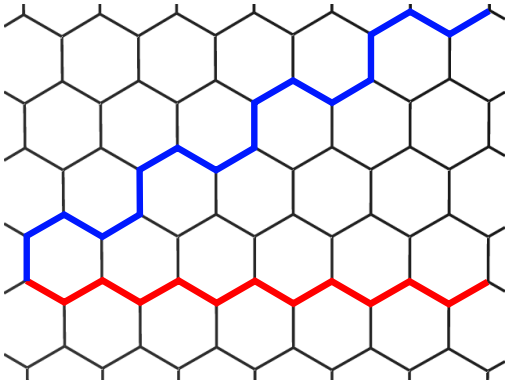

Figure 5.1: Crystallographic axes in a graphene sheet. The black lines show the honeycomb lattice of graphene and the blue (red) line depicts the armchair (zigzag) high symmetry direction.

GNRs (ZGNRs). The width of GNRs is conventionally denoted by the number of carbon dimers per unit cell. Figure 5.2 shows the elementary cells of N-AGNRs (Fig. 5.2(a) and N-ZGNRs (Fig. 5.2(b) each with one dimer being highlighted in green. The outermost carbon atoms in Fig. 5.2 are saturated with hydrogen. In order to describe pristine GNRs, the passivation with hydrogen is commonly assumed since a pure carbon edge would yield dangling bonds leaving it chemically unstable. It should be noted that divers configurations of hydrogen saturation have been shown to be stable depending on the edge type [23].
Various approaches to produce GNRs have been suggested ranging from lithographic methods to the longitudinal unzipping of CNTs [94–99]. However GNRs prepared with these top-down techniques have in common one disadvantage well-known from the production of CNTs: It is hard to extract ribbons of a defined edge structure and width,

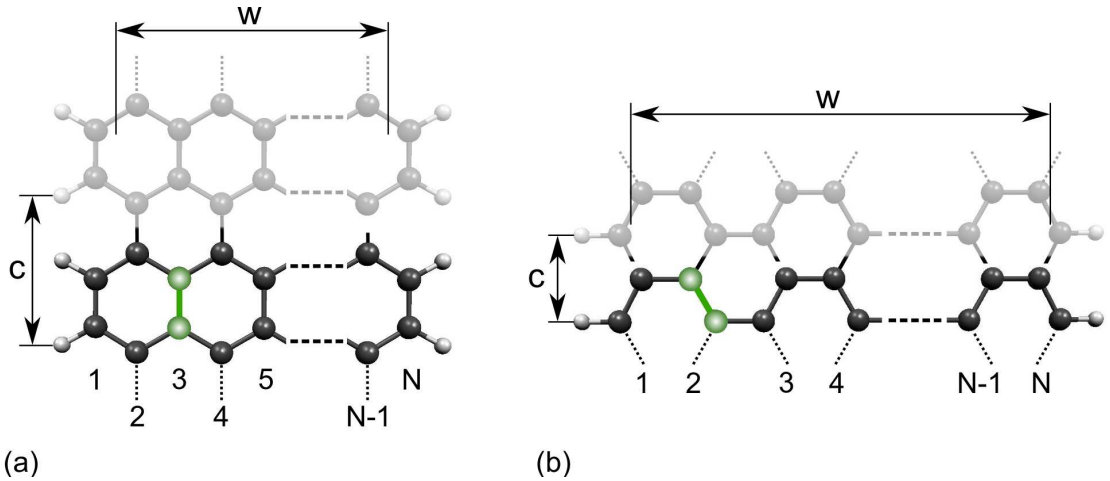

Figure 5.2: Structure of (a) a N-AGNR and (b) a N-ZGNR. In each case, carbon (hydrogen) atoms of one unit cell are shown in black (white), whereas the the neighboring unit cell is indicated in gray and white, respectively. One carbon dimer line of each unit cell is emphasized in green.

similar to the typical chirality distributions in CNT outputs. Even though annealing procedures can help reconstructing ribbon edges, the above described methods yield too unspecific compounds given that the exact width and edge structure essentially determine the basic properties of GNRs which will be described below [100]. In this context, the recent successful synthesis of a specific 7-AGNR with defect-free edges and a well-defined width by Cai *et al.* is a major breakthrough [21]. However, the reported bottom-up method is an exception, as other GNRs so far cannot be prepared in a comparably accurate way.

5.2 Electronic properties

GNRs exhibit pronounced analogies to CNTs as a quantization condition perpendicular to the axis holds in both quasi one-dimensional structures. Thus, in the simplest approximation the electronic spectrum of GNRs can be derived from zone folding of the graphene band structure analogous to the case of CNTs. While the cylindric structure of CNTs implies continuous standing waves along the circumference, *i.e.*, circular boundary conditions, fixed boundary conditions must be applied at the GNR edges. In the following, we define the ribbon width as the average distance of all outermost carbon atoms along the unit cell (see Fig. 5.2). Ideally, *i.e.*, cutting a ribbon from graphene without relaxing it, the width of a N-AGNR is

$$w(N\text{-AGNR}) = \frac{a}{2}(N-2) \tag{5.1}$$

and that of a N-ZGNR is

$$w(N\text{-ZGNR}) = \frac{\sqrt{3}a}{2}(N-1), \tag{5.2}$$

where a is the lattice constant of graphene. Obviously, the perpendicular components of all wave functions with respect to the GNR axis must fulfill the condition

$$n \cdot \frac{\lambda_{\perp,n}}{2} = w \qquad \text{or} \qquad k_{\perp,n} = \frac{\pi}{w} \cdot n, \qquad n \in \mathbb{N}. \tag{5.3}$$

Hence, the Brillouin zones of GNRs consist of equidistant lines separated by

$$\Delta k(N\text{-AGNR}) = \frac{2\pi}{a(N-2)} \tag{5.4}$$

and

$$\Delta k(N\text{-ZGNR}) = \frac{2\pi}{\sqrt{3}a(N-1)}, \tag{5.5}$$

respectively. Using the examples of a 7-AGNR and a 7-ZGNR, this condition is visualized in Fig. 5.3 projected on the Brillouin zone of graphene. In this picture, all those GNRs are metallic whose allowed states include the K (K') points, *i.e.*, the Fermi crossings of graphene. This comprises all ZGNRs as their maximum $k_{\perp,n}$ coincides with the K'MK

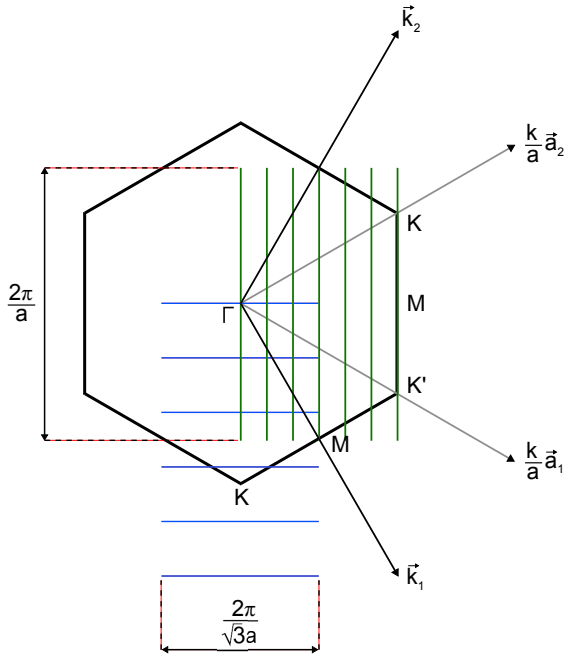

Figure 5.3: Brillouin zones of a 7-AGNR (blue lines), a 7-ZGNR (green lines), and graphene (solid black lines). $\vec{a}_{1,2}$ denote the lattice vectors of graphene and $\vec{k}_{1,2}$ are their counterparts in k-space.

line:

$$\overline{\Gamma\mathrm{M}} = \frac{2\pi}{\sqrt{3}a} = k_{\perp,N-1}(\mathrm{ZGNR}) \tag{5.6}$$

Accordingly, the Brillouin zone of the 7-ZGNR in Fig. 5.3 exhibits 7 lines including the one at $k_\perp = 0$. In case of AGNRs the Brillouin zone contains the K point only if

$$k_{\perp,n}(\mathrm{AGNR}) = n \cdot \frac{2\pi}{a(N-2)} \stackrel{!}{=} \overline{\Gamma\mathrm{K}} = \frac{4\pi}{3a} \tag{5.7}$$

which translates to N=3p+2, with p being integer (compare Eq. 5.2). In the above approximation of an ideal graphene-like geometry, these N-AGNRs are found to be metallic while all others are predicted to have a band-gap.
However, two effects substantially modify the findings described so far. First, carbon atoms in relaxed GNRs are not all pairwise equivalent as in graphene, but show different bond lengths in the center and at the edge of the ribbon. It turns out that in AGNRs, C-C bonds parallel to the ribbon axis are shorter close to the edges than in the center [19]. This modifies the boundary condition at the edges in such a way that a band-gap opens also in N-AGNRs with N=3$p+2$ which are metallic in the zone folding picture. Thus, all actual AGNRs are semiconducting. Relaxed ZGNRs show a comparable geometric effect. These ribbons do not have C-C bonds parallel to the ribbon axis, but we find C-C bonds formed by dimer lines as defined in Fig. 5.2(b) to be shortened towards the edges. Nonetheless, this does not seem to have an impact as severe as in case of AGNRs. The dominating factor in ZGNRs is rather the appearance of ferro-magnetically ordered spin states along the ribbon edges [19, 101]. When the spin degree of freedom is taken into account, net magnetized edges prove to be energetically favorable. This involves a shift

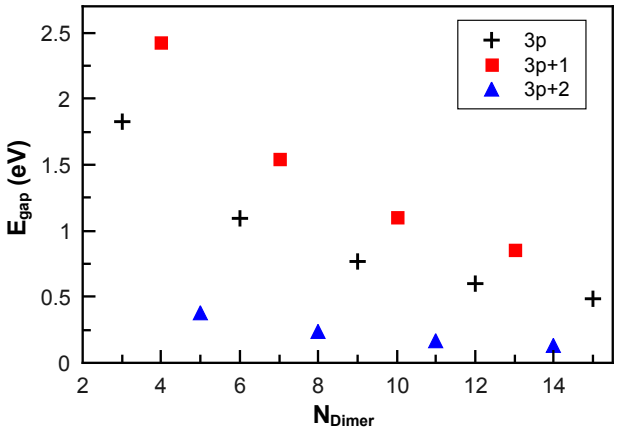

Figure 5.4: Band-gaps of N-AGNRs with $N = 3, ..., 15$ from *ab initio* calculations.

in the spin polarized density of states at the edges such that a band-gap opens in all ZGNRs [101]. The bottom line is that there are *no* metallic armchair or zigzag GNRs.

The size of the band-gap of a given GNR strongly depends on its width. Figure 5.4 shows the band-gaps of relaxed AGNRs as a function of the number of carbon dimers per unit cell. The data presented here, which are taken from our DFT calculations in the local-density approximation, agree very well with previous reference work [19, 88]. An overall trend of decreasing band-gaps with increasing ribbon width is evident. In the limit of very wide ribbons, the high density of allowed values for $k_{\perp,n}$ induces a vanishing band-gap. Furthermore, the gap values of N-AGNRs are clearly subject to N either being $3p$, $3p + 1$, or $3p + 2$, where $p \in \mathbb{N}$. This pronounced family dependence may be interpreted in terms of the above discussed zone folding approximation, which led to N-AGNRs with $N = 3p + 2$ being metallic. Note that this family still exhibits the smallest band-gaps of all AGNRs. A slightly different behavior is found for ZGNRs, which do not show any family pattern. Their maximum band-gaps are about 0.35 eV and thus much smaller than those of narrow AGNRs [19]. As expected, growing ribbon widths diminish the energy gaps of ZGNRs. We did not investigate the band-gaps of ZGNRs systematically and would like to refer the interested reader to Son *et al.* [19].

5.3 Vibrational characteristics

The phonon spectrum of GNRs shows significant analogies to that of CNTs. Since both systems are one-dimensional subspecies of graphene, their fundamental vibrations are closely related to those of graphene. This is reflected most obviously in the high-energy band around 1600 cm^{-1} formed by the two-dimensional E_{2g} mode in graphene. These optical vibrations are doubly degenerate at the Γ point in intrinsic graphene, but split if the system becomes anisotropic, *e.g.*, under strain or when a unique axis is specified, like in the case of GNRs and CNTs [13, 102, 103]. In GNRs with armchair and zigzag edges, the two resulting modes show in-plane atomic displacements axial and perpendicular to the ribbon axis and are therefore commonly referred to as longitudinal (LO) and transversal optical (TO) mode (see Fig. 5.5(b) and (c)). It should be noted that an

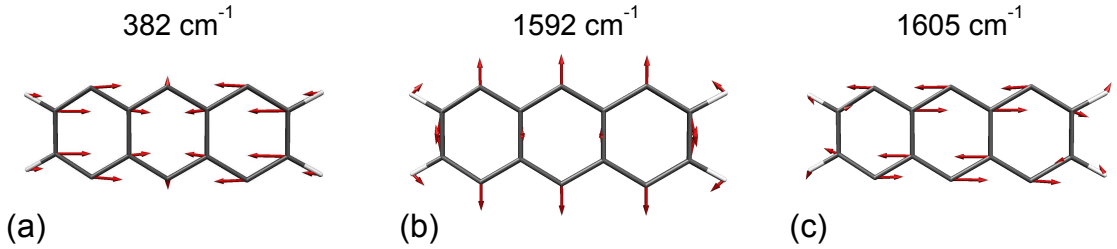

Figure 5.5: Eigenvectors and corresponding phonon frequencies of (a) the BLM, (b) the longitudinal, and (c) the transversal optical fundamental mode of a 7-AGNR at the Γ point. Carbon (hydrogen) atoms are shown in black (gray) and atomic displacements are marked by red arrows.

alternative notation is frequently used throughout the literature referring to the LO and TO modes as G^- and G^+, respectively. For all AGNRs and ZGNRs, the TO was found at higher frequencies than the LO [104]. Furthermore, it was shown that both the LO and TO energies in AGNRs behave according to the family classification described in Sec. 5.2. As expected, the LO and TO frequencies converge to the value of the graphene E_{2g} mode in very wide ribbons.

Gillen *et al.* showed that the Γ point vibrations of GNRs contain six fundamental modes which represent the zone center phonons of graphene [104]. Beside the LO and TO modes, these are the ZO mode, in which neighboring carbon atoms perform out-of-plane vibrations in opposite directions, and three acoustic phonons. All other vibrations are overtones of these fundamentals in terms of a modulation of the eigenvector by transversal standing waves. These waves correspond to the allowed k states derived from the boundary conditions of zig-zag and armchair edges in Sec. 5.2. That way, the harmonics of the GNR fundamental vibration can be mapped onto the respective branches of the phonon dispersion of graphene [104].

The first overtone of the transversal acoustical mode arouses special interest. As shown in Fig. 5.5(a), its displacement pattern represents a totally symmetric breathing motion of the whole ribbon resembling the radial breathing mode in CNTs. It is usually denoted as breathing-like mode (BLM). The energy of the BLM depends inversely on the width of the GNR in close analogy to the radial breathing mode in CNTs [13, 65, 105, 106]. Since the BLM is Raman active in ZGNRs and AGNRs, this relation provides a straightforward way to determine the width of a GNR *via* Raman spectroscopy [106]. *Ab initio* studies of scattering intensities predict that the BLM and the high energy band are of central importance in the Raman spectrum of GNRs, which is confirmed in a first experimental characterization of precisely synthesized 7-AGNRs [21, 107]. Cai *et al.* further found strong Raman bands between 1200 and 1350 cm^{-1}. These modes most likely stem from either the LO, TO, or LA branches, which all have Raman active overtones in this frequency range around the K point of graphene [104, 106].

5.4 Summary

The properties of GNRs are largely governed by the ribbon width and the edge configuration. While common top-down production methods still yield inaccurate results in this respect, one specific type of armchair ribbon has been synthesized in a precise way. This is essential in view of possible applications as, *e.g.*, a small deviation in ribbon width has drastic effects on basic properties of the GNR. The electronic band structure of GNRs can be approximated from the graphene Brillouin zone by means of zone folding. In this picture, one third of the AGNRs and all ZGNRs would be semimetallic which turns out to be not correct. *Ab initio* calculations show that all AGNRs and - taking into account spin polarization - also ZGNRs have at least a small band-gap. Furthermore, the band-gaps of AGNRs follow a clear family behavior suggesting a classification into three groups depending on the number of carbon dimers per unit cell. This family dependence is also reflected in the high-energy band vibrations of AGNRs. ZGNRs, in contrast, can not be classified in a similar way. In analogy to the RBM in CNTs, GNRs exhibit a breathing-like eigenmode, which relates to the ribbon width in the same way as the RBM does to the tube diameter. The BLM thus could potentially play a key role in the experimental characterization of GNRs.

6 Strain in graphene nanoribbons

Parts of this chapter were published in Ref. [82].

A major part of possible applications most probably will include GNRs deposited on a substrate. In these cases, lattice mismatch, *i.e.*, different lattice constants of the substrate crystal and the GNR, causes strain. Since the thickness of graphene and GNRs is a single atomic layer, interface-strain induced variations in the electronic and vibrational structure are expected to play a greater role than in bulk materials. A further motivation to explore the effect of strain is the prospect of tuning certain properties of GNRs intentionally. Together with the exploitation of other influences like defects, functionalization, and edge type, this may widen the range of applications substantially. In this work, we concentrate on strain along the nanoribbon axis as it is assumed to be most relevant in practice. In the following, we examine how uniaxial strain affects the geometric (Sec. 6.1), the electronic (Sec. 6.2), and the vibrational (Sec. 6.3) characteristics of AGNRs.

6.1 Structural effects

We introduced strain in our simulations by fixing the lattice constant c of a given ribbon to values differing from the unstrained case and relaxing the structure within this constraint. We simulated a series of strain magnitudes of up to 5 % for each ribbon, both in tensile and compressive mode. Being exposed to tensile strain, GNRs - like any other material - shrink in the lateral dimension. For axial strain this implies a width variation which in turn causes deviations in the boundary conditions for the allowed

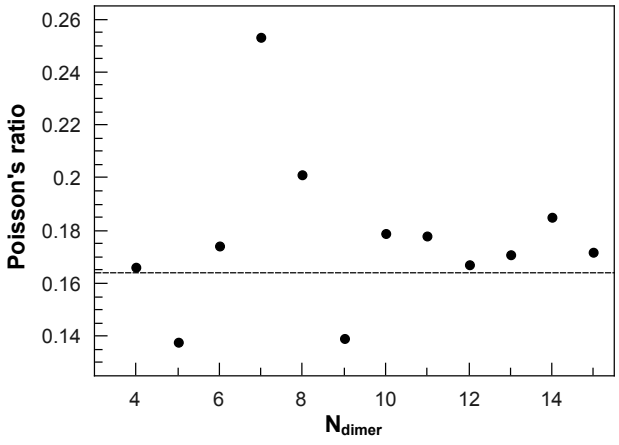

Figure 6.1: Poisson's ratio of various N-AGNRs under uniaxial strain. The dashed line denotes the value derived for graphene [108].

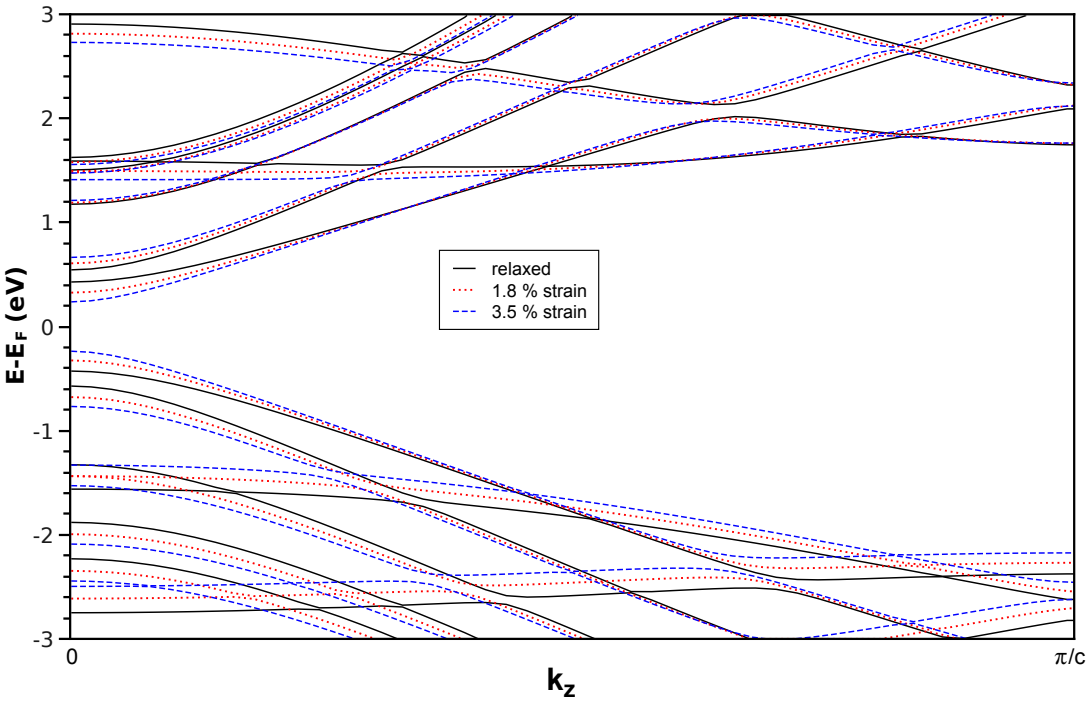

Figure 6.2: Band structure of a uniaxially strained 13-AGNR. Black solid lines denote the unstrained case and red dotted (blue dashed) lines correspond to a ribbon under 1.8 % (3.5 %) tensile strain along the ribbon axis.

k states of the GNR. The ratio of the transversal response of a system to strain and the strain itself is known as Poisson's ratio ν. In case of GNRs, this quantity may be expressed as the relative variations in width and lattice constant c. Figure 6.1 displays the values found for ν in AGNRs as a function of their width. As the Poisson's ratio of a GNR is sensitive to the amount of strain, we present here the average of the values derived in the mentioned strain range. While the mean Poisson's ratio of different narrow ribbons oscillates considerably, it tends to converge to the value of 0.164 found for graphene already from $N = 10$ onwards [108]. The family behavior of AGNRs, which was introduced in Chap. 5, does not seem to be reflected in these results.

6.2 Band structure of strained nanoribbons

The geometric distortion has a severe impact on the electronic structure. Figure 6.2 shows the band structure of a 13-AGNR in the relaxed configuration and at two different strain levels. First of all, it is apparent that pairwise connected valence and conduction bands shift in opposite directions, either further apart or closer together.

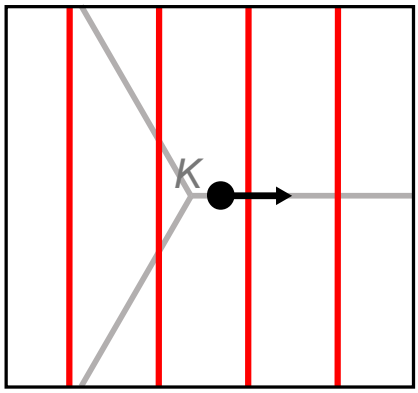

Figure 6.3: Diagram of a section of the Brillouin zones of graphene and AGNRs around the K point. Light gray lines indicate the edges of the Brillouin zone of graphene, vertical red lines denote the allowed electronic states of AGNRs. The Dirac cone is shown as black spot which shifts along the high symmetry line under strain.

Whereas the highest π band energy increases, the second highest π band drops in energy. This corresponds to a declining lowest π^* band and a rise in energy of the second lowest unoccupied band. The opposite shift of the two lowest electronic Γ point band-to-band transitions can be interpreted in terms of the zone folding picture taking into account reports on the strain-influenced band structure of graphene [108]. Calculations of uniaxially strained graphene show the Dirac cone to shift away from the K point. In the special case of strain along the armchair or zigzag direction, it shifts along the high-symmetry line Γ-K-M [108]. This motion of the graphene Dirac cone is schematically shown in Fig. 6.3 projected on the Brillouin zone of AGNRs. As discussed in Sec. 5.2, the allowed states of AGNRs are given by equally spaced lines perpendicular to the line Γ-K-M. Thus, strain makes the Fermi crossing move between the quantized states $k_{\perp,n}$ of an AGNR. The consequence of this relation is evident in the exemplary band structure of a strained 13-AGNR shown in Fig. 6.2. Obviously, tensile strain makes the Dirac cone approach the nearest allowed AGNR state resulting in a diminished lowest π^* and an increased highest π band energy. At the same time, the Dirac cone moves away from the second nearest allowed line, which is located on the other side. This implies an up-shift (down-shift) of the corresponding second lowest π^* (second highest π) band which can be seen in Fig. 6.2. Hence, qualitatively, the band structure of the strained 13-AGNR can be explained by considering strain in 2D graphene.

When evaluating the strain-induced band-gap shifts of various AGNRs, we find a fundamentally different behavior for ribbons belonging to different families. Figure 6.4 shows the relation between gap and strain for N-AGNRs with N =13, 14, and 15, which belong to a different family each. For $N = 13$ ($N = 3p + 1$), we see a declining band-gap under tensile strain as discussed above. At a compressive strain of about 1.4 %, the gap of this ribbon reaches a maximum before reducing again under further compression. Within the interpretation given above, the gap maximum occurs when the Dirac cone is located between two allowed k states in such a way that the energies of the direct electronic transitions at these k points are identical. Only in the pure geometrical picture and assuming perfect circular-symmetric cones, this coincides with the Dirac cone being equally distant from the two neighboring $k_{\perp,n}$. However, due to the trigonal warping of the graphene electronic dispersion around the K point, the maximal gap is expected

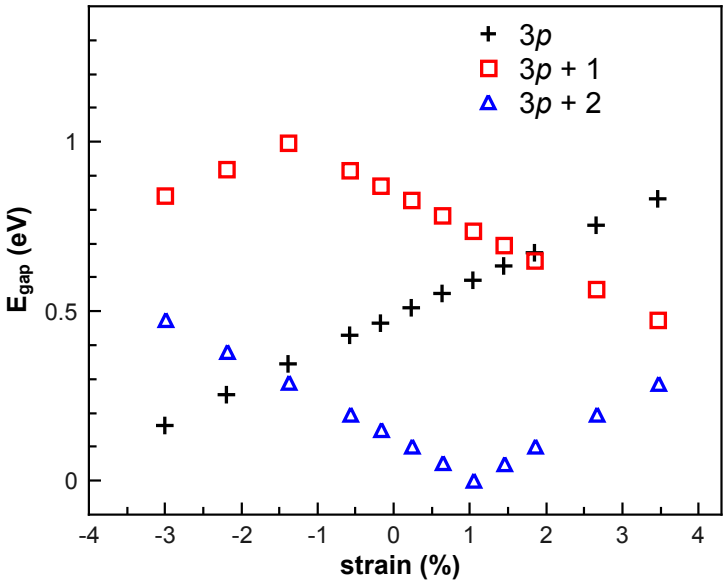

Figure 6.4: Band-gap energy depending on the applied strain for N-AGNRs with $N = 13$ (red squares), $N = 14$ (blue triangles), and $N = 15$ (black crosses). These ribbons belong to the three different families AGNRs are commonly classified in. Negative (positive) strain values denote compressive (tensile) strain.

for the Dirac cone being slightly closer to the nearest $k_{\perp,n}$ on the line K-Γ than to the nearest allowed state in the direction K-M [109].

The band-gap of a 14-AGNR ($N = 3p + 2$) decreases with the same rate as that of a 13-AGNR at small amounts of tensile strain. At 1 % tensile strain, the band-gap vanishes, but reopens if the ribbon is strained more. This can be attributed to a crossing of the Dirac cone across an allowed state of the ribbon as indicated by the black arrow in Fig. 6.3. If the Fermi crossing is driven away from the zone-folding derived AGNR state by additional strain, the gap opens up again.

Whereas the band-gap strain dependencies of 13- and 14-AGNRs mark the maximal and minimal gap in the investigated strain range, the band-gap of a 15-AGNR ($N = 3p$) shows a continuous shift in a large range. Based on the previous considerations, an equivalent behavior is expected at turning points that lie outside the strain range considered here. The strain-shifted band-gaps of all other N-AGNRs down to $N = 3$ strictly show the same family pattern as the three examples shown in Fig. 6.4.

An interesting aspect of the results shown in Fig. 6.4 is the fact that all shifts are perfectly linear between the extreme points. This originates in the locally linear dispersion of the π and π^* bands in graphene. We find shift rates of $\pm 0.1\,\mathrm{eV}/\%$ for all examples shown here, which in principle allows a well controllable tuning of the band-gap. This could be useful for applications like strain sensors or nanoelectronic devices requiring a certain gap energy. It should be noted that our computational approach does not include many-body effects [110, 111]. However, since the alterations of the band structure presented above are evidently induced by geometric deformation, we expect the effects described here to be conserved despite a scaling of the quasiparticle energies due to electron-electron interaction. Our results are in good accordance with a recent tight-binding study on the band structure of strained GNRs [112]. In that work, which considers strain of up to 15 %, oscillations of the band-gap depending on the strain are

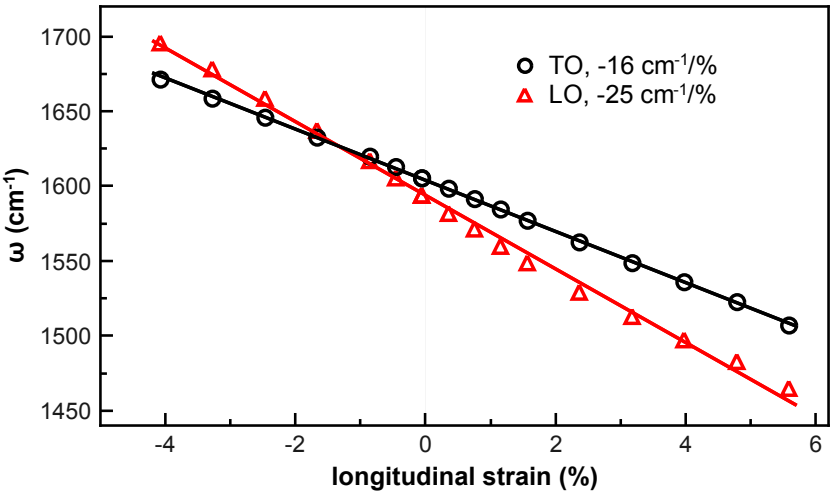

Figure 6.5: Strain-induced shift of the LO and TO phonon frequencies in a 7-AGNR.

reported. Furthermore the authors introduce a tight-binding based perturbation model which reproduces main features of the band-gap-strain dependence [112].

6.3 Phonon shifts under strain

As outlined in Sec. 5.3, the most characteristic vibrations of GNRs are the LO and TO modes which originate from the graphene E_{2g} phonon, and the breathing-like mode (BLM). We therefore restrict the following systematic investigation of the impact of strain to these three phonons. As we consider strain in axial direction, the above definition of the attributes longitudinal and transversal holds also with respect to the strain direction.

Figure 6.5 displays the shift of the LO and TO frequencies in a strained 7-AGNR. Like in graphene both modes depend linearly on the applied strain over a wide range [108]. While the shift rate of the TO mode of $16\,\mathrm{cm}^{-1}/\%$ agrees well with findings on graphene, the LO frequency of the investigated ribbon is altered much less than it is in graphene. To obtain a better picture of this issue we compare the shift rates of different AGNRs and graphene in Fig. 6.6. Strain affects the LO energy stronger than that of the TO for every ribbon in accordance with the results on graphene [108]. The shift rates of both modes clearly reflect the family behavior of AGNRs although this effect is more pronounced in case of the LO. In the limit of large ribbon widths the shift rates of both phonons are expected to converge to the values found for graphene. Concerning the LO mode, the $N = 3p+2$ family exhibits slightly stronger shifts than graphene. In contrast, the two other families show smaller, but steadily growing rates with increasing N. The family with the most strain-sensitive LO frequency, $N = 3p+2$, yields by far the lowest LO frequency in the unstrained case [104]. This is attributed to a Kohn anomaly effect related to the small band-gap of this AGNR family [113].

The TO phonon shifts more uniformly in AGNRs belonging to different families. All but three narrow ribbons show the TO mode being more sensitive to strain than it is

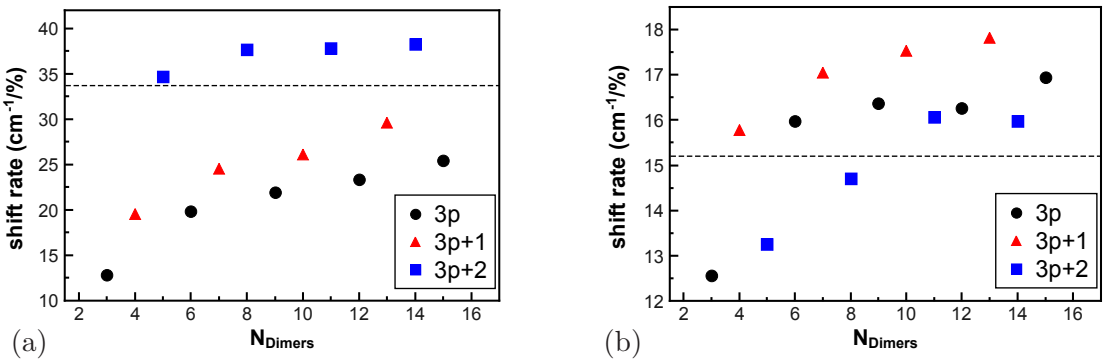

Figure 6.6: Shift rates of (a) the LO and (b) TO frequencies in uniaxially strained AGNRs of different widths. Values derived for $N-$AGNRs with $N = 3p$ are shown as black circles, with $N = 3p + 1$ as red triangles, and with $N = 3p + 2$ as blue squares. The black dashed lines mark the shift rates in graphene [108].

in graphene. For wider ribbons, the TO shift rates of all families quickly converge to a margin close to the graphene value. However, the values shown in Fig. 6.6(b) seem to approach a slightly higher limit than the shift rate in graphene. This discrepancy can be partially attributed to the different approximation being used in the simulation of strained graphene. In the work referred to above, the exchange-correlation functional was approximated within the GGA as implemented in the DFT code QUANTUM-ESPRESSO, which is known to yield softened phonon frequencies [114, 115]. This was indeed accounted for by scaling all frequencies such that the unstrained E_{2g} frequency matches the experimentally determined value of $1580\,\mathrm{cm}^{-1}$ in the same way as we do it in this work (*cf.* Sec. 2) [108]. However, we still find somewhat higher shift rates when calculating strained graphene with the computational method used for AGNRs. The deviation amounts to $0.9\,\mathrm{cm}^{-1}/\%$ in case of the TO phonon and thus reduces the apparent mismatch between the converging AGNR shift rates and the limit value in Fig. 6.6(b). A much smaller deviation of $0.4\,\mathrm{cm}^{-1}/\%$ between our method and Ref. [108] is found for the LO mode in graphene. Hence, there are no significant changes to the above discussion of Fig. 6.6(a). The large shift rates of both LO and TO modes allow to determine the strain of an AGNR sample experimentally.

Finally, we present our results on the BLM in AGNRs. For narrow ribbons of up to $N \approx 11$ we observe a linear dependence of the Raman shift on the strain. At larger widths the frequency variation falls below the computational accuracy. Like in case of the LO and TO, tensile (compressive) strain softens (hardens) the BLM frequency. As presented in Fig. 6.7, the BLM of small AGNRs shifts considerably whereas this rate decreases rapidly with growing ribbon width. This finding agrees well with the quickly declining frequency of the BLM with increasing width.

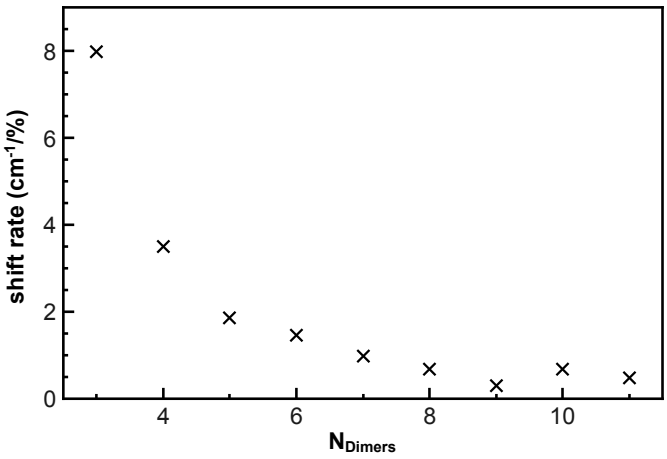

Figure 6.7: Shift rate of the BLM energy under strain shown for AGNRs of varying width.

6.4 Summary

Potential applications of GNRs make strain an inevitable topic which we find to offer in turn interesting opportunities. Stretching a GNR along its axis induces severe alterations of its band-gap. All AGNRs show a linear shifting gap under strain in a range which depends on the family the ribbon is classified in. At sufficiently high strains, ribbons of all families reach maximal and vanishing gaps. This behavior is in perfect accordance with reports on strained graphene and can be explained within the zone folding approximation. Prominent phonons of AGNRs are strongly affected by strain as well. The high-energy modes yield shifts similar to those found in graphene. However, the family classification of AGNRs plays an important role in this respect, too. While the LO and TO modes may be used to measure the strain *via* Raman spectroscopy, the BLM shows significant shift rates only in very narrow ribbons.

7 Edge functionalized nanoribbons

Parts of this chapter were published in Ref. [83].

The edges of GNRs hold a great potential for various chemical modifications since cutting a graphene sheet into ribbons leaves dangling bonds. In the previous discussions, we assumed that the GNR edges are saturated with hydrogen atoms. However, typical lithographic fabrication of GNRs includes treatment with *e.g.*, oxygen plasma, which makes it very likely that GNRs are passivated other than with hydrogen [94, 96, 116]. In fact, diverse functional groups may be side products of the manufacturing process. In this case it is crucial to know how the physical properties of the GNR are affected. Furthermore, functionalization might be introduced intentionally in order to tune certain properties.

Previous works on this topic focus on ZGNRs, which have edge states near the Fermi-level when passivated with hydrogen as reviewed in Sec. 5.2 [22, 24, 117, 118]. The electronic structure of ZGNRs is thus very sensitive to edge modifications. To the best of our knowledge, edge functionalization of AGNRs has rarely been considered in previous reports. Apart from Vanin *et al.*, who restrict their investigation concerning functionalized armchair edges to the stability of edge configurations, only two works address the impact on the physical properties of AGNRs [119]. Cervantes-Sodi *et al.* do not expect major effects due to missing impurity levels in the band-gap [24]. In contrast, our results suggest that other mechanisms like functionalization-induced strain play an important role, too. A recent study which concentrates on mechanical parameters of edge functionalized AGNRs confirms our findings [120].

In this thesis, we study the influence of edge passivation with hydroxyl groups on the structural, electronic, and vibrational properties of AGNRs of varying width. We present deviations in the geometries of functionalized ribbons compared to their hydrogen terminated counterparts in Sec. 7.1. We further demonstrate that passivation of the ribbon edges with OH-groups is energetically favorable over H passivation, with a high degree of functionalization being likely (Sec. 7.2). Section 7.3 deals with the effect of hydroxyl functionalization on the electronic band structure of AGNRs. We find a strong shift of the band-gap with increasing degree of functionalization, which is of great interest with regard to possible applications such as GNR-based transistors. The impact of functional groups on characteristic vibrational modes is described in Sec. 7.4. Besides the characteristic Raman active phonons of GNRs, we also consider modes specific to the hydroxyl groups. As will be discussed below, our findings suggest that the degree of functionalization may be determined by means of vibrational spectroscopy.

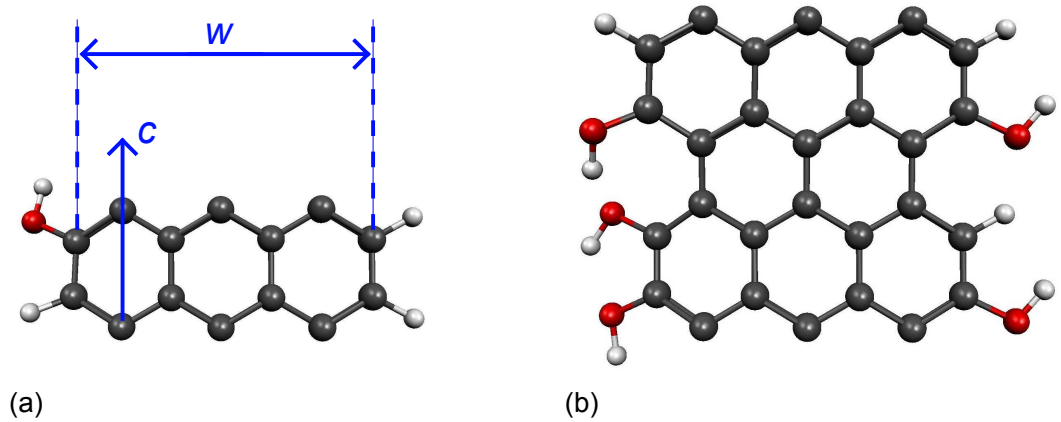

Figure 7.1: (a) Unit cell of a 7-AGNR with one hydroxyl-passivated edge atom. Carbon atoms are shown in black, oxygen atoms in red (gray), and hydrogen atoms in light gray. The blue (gray) arrows indicate the lattice constant c and the ribbon width w. (b) Super-cell of a 7-AGNR allowing a greater variety of configurations of edge functionalization. The example shown here has a degree of edge functionalization of 5/8.

7.1 Geometric effects

The addition of hydroxyl groups to the edges of AGNRs induces considerable geometric effects on the ribbon itself as discussed in the following. To get a clear picture, we simulated different configurations with varying degree of functionalization, *i.e.*, with varying linear density of the OH groups. Apart from calculating a single unit cell, we also considered a super-cell containing two unit cells as shown for the example of a 7-AGNR in Fig. 7.1. This allows the simulation of more intermediate values of the degree of functionalization. We find the planar configuration of AGNR and hydroxyl group to be metastable in contrast to reports on hydroxyl-functionalized ZGNRs [24]. A bending of the functional groups out of the ribbon plane is energetically favorable for all investigated AGNRs. For a single unit cell (Fig. 7.1a) our results show an opposite displacement of

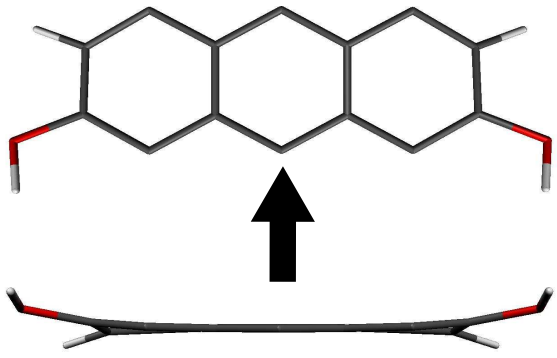

Figure 7.2: Out-of-plane arrangement of the functional groups of a 7-AGNR. The bottom picture shows the view along the ribbon axis as indicated by the black arrow.

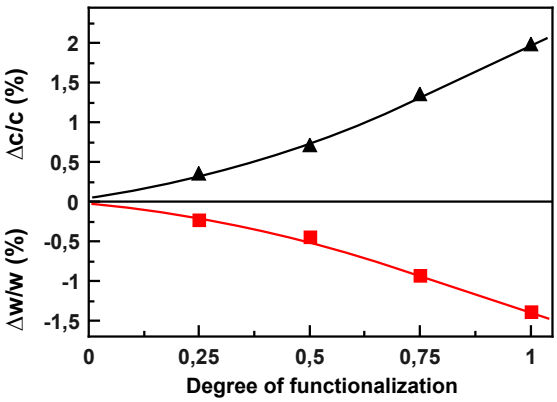

Figure 7.3: Relative variation of the lattice constant (black triangles) and the ribbon width (red squares) in a 7-AGNR for different degrees of functionalization. Solid lines are guides to the eye.

neighboring carbon edge atoms under functionalization (see Fig. 7.2). In case of the $1 \times 1 \times 2$ super-cell, the lower translational symmetry leads to an opposite bending of entire carbon hexagons at one edge if at least one functional group is involved. The existence of these edge-localized static ripples has recently been confirmed by Wagner *et al.* for an identical super-cell size as in our calculations [120]. A further expansion of the super-cell might possibly yield ripples of longer range. However, the simulation of these large systems remains a challenging computational task.
Apart from the out-of-plane arrangement, the edge passivation with OH groups causes a stretching along the ribbon axis accompanied by a squeezing across the width. The relative variations of the lattice constant c and the ribbon width w of a hydroxylized 7-AGNR are shown in Fig. 7.3. Obviously the strain on the unit cell increases considerably with growing degree of functionalization. Although the total width of the ribbon is strongly decreased, the C-C bonds along the width are shortened only close to the edges. In contrast, central C-C bonds in this direction are even longer in the functionalized case than in the pristine ribbon. It turns out that the overall deformation of the unit cell of functionalized ribbons is due to a decrease of the bond angles along the width by about 2°. In summary, we observe remarkably high Poisson ratios $\frac{\Delta w/w}{\Delta c/c}$ of *e.g.*, 0.65 for the 7-AGNR. It should be noted that this value is much higher than the Poisson ratios of uniaxially strained ribbons (*cf.* Fig. 6.1). This distinction has to be taken into account when comparing functionalized and strained AGNRs as discussed in Sec. 7.3.

7.2 Chemical stability

Since the thermodynamic stability of the given structures is crucial for any experimental realization, we calculated the binding energy per OH group E_B for all investigated configurations as follows:

$$E_B = \frac{1}{N_f}\{E(\mathrm{GNR}_f) - [E(\mathrm{GNR}_{H-term}) + N_f \cdot E(\mathrm{O})]\}.$$

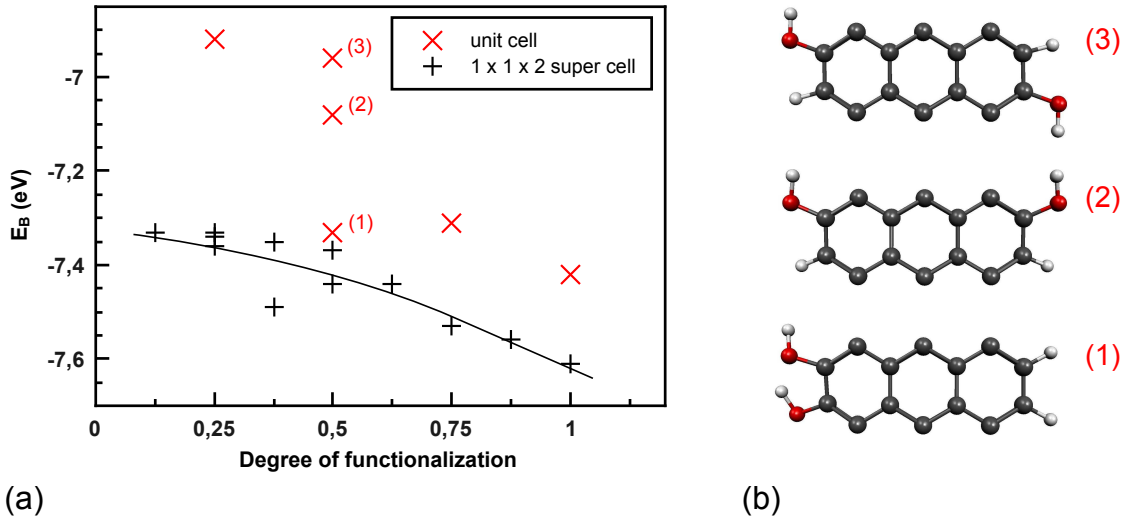

Figure 7.4: (a) Binding energy per hydroxyl group depending on the degree of functionalization in a 7-AGNR. Red diagonal crosses represent data derived from calculations of one unit cell. Black crosses are values found for a super-cell containing two unit cells along the ribbon axis. The solid black line is a guide to the eye. (b) Three inequivalent configurations with two OH groups per unit cell.

$E(\mathrm{GNR}_f)$ and $E(\mathrm{GNR}_{H-term})$ are the total energies of a ribbon passivated with N_f hydroxyl groups and a fully H-terminated ribbon, respectively. $E(\mathrm{O})$ represents the total energy of an isolated oxygen atom. The resulting binding energies from calculations of a hydroxylated 7-AGNR in both the super-cell and unit cell approaches are shown in Fig. 7.4(a). First of all, we observe a substantial energy gain under functionalization in agreement with studies of the same effect in ZGNRs [22]. Furthermore, the binding energy clearly increases with growing degree of functionalization. Therefore a fully functionalized ribbon represents the most stable configuration as found for ZGNRs [22]. Figure 7.4(a) further shows consistently higher energy gains for super-cell simulations. This is in agreement with the above discussed enhanced possibilities for an out-of-plane arrangement - and thus for the energy minimization - at lower translational symmetry restrictions.
In many cases it is possible to construct inequivalent configurations with the same number of OH groups which then yield differing binding energies. This effect is most pronounced in the unit cell approach for a degree of functionalization of 0.5. The corresponding three inequivalent structures of a half functionalized 7-AGNR are presented in Fig. 7.4(b). A complete hydroxylation of one edge is obviously by far more stable than both edges being half functionalized, whereas the two possibilities of the latter case yield a smaller difference. The particularly high stability of a fully saturated edge indicates the occurrence of hydrogen bonds between neighboring OH groups which have also been

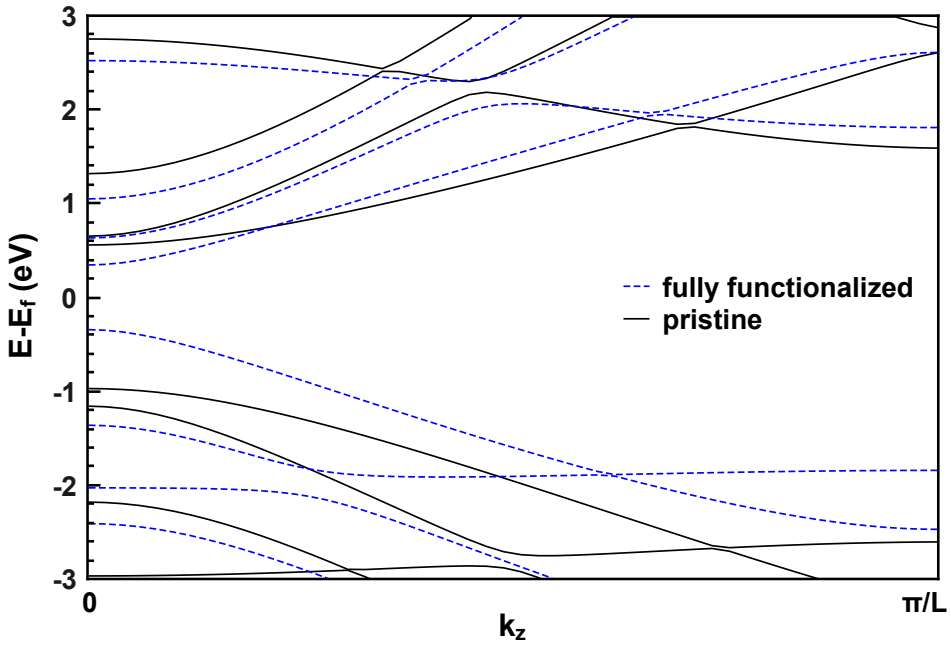

Figure 7.5: Band structures of an H-terminated 7-AGNR (solid black line) and a 7-AGNR with every edge atom being hydroxyl-passivated (dashed blue line).

predicted for hydroxylized ZGNRs by Hod et al. [22]. The results presented here on the basis of a 7-AGNR can be transferred to all studied ribbon widths which cover a range of N-AGNRs with $N = 5, ..., 10$. In particular, all ribbons show a strong affinity to being fully hydroxylated. In cases of different structures with the same number of functional groups, we find a clear energetic preference of single edge functionalization in all studied ribbons.

7.3 Electronic properties

A high potential of various edge modifications for altering the band structure of ZGNRs has been reported previously [22, 24, 117]. In contrast to ZGNRs, AGNRs do not have edge states near the Fermi level which are obviously sensitive to edge functionalization. Nevertheless, our studies reveal drastic modifications of the band structure of AGNRs under edge functionalization with OH groups. In the following, we first analyze the example of a 7-AGNR before addressing the width dependence of our findings.
Figure 7.5 shows the electronic bands of a pristine and a maximally functionalized 7-AGNR. The most striking feature is the shift of the valence and conduction bands which leads to a strong decrease of the band-gap. We find a linear dependence of the band-gap on the degree of functionalization as presented in Fig. 7.6. Inequivalent con-

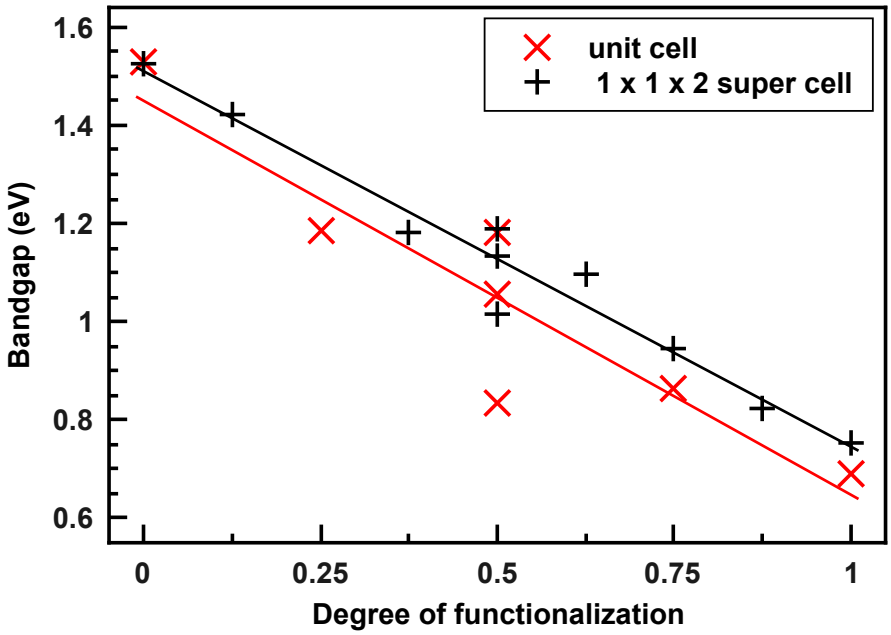

Figure 7.6: Band-gap of hydroxyl-passivated 7-AGNRs depending on the degree of functionalization. Red (gray) vertical crosses and black crosses represent band-gap energies found for calculations of a unit cell and for a $1 \times 1 \times 2$ super-cell, respectively.

figurations with the same degree of functionalization give different gap values in analogy to the discussion of the total energy in Sec. 7.2. Furthermore, simulations of one unit cell yield slightly lower band-gaps than super-cell calculations. Nevertheless both approaches result in a perfectly matching linear shift of the band-gap with increasing degree of functionalization. Altogether the band-gap of 7-AGNRs can be reduced by $\sim 0.7\,\mathrm{eV}$ or almost 50 % by means of edge functionalization with hydroxyl groups. This is highly interesting with regard to nano-electronic applications as it offers in principle a tunable band-gap over a wide range. We did not take into account electron-electron and electron-hole interaction [110, 111]. However, we believe that the general behavior will remain valid, as the dominant contribution to the band-gap shift is from geometrical effects as discussed in the following.

The observed band-gap dependence clearly resembles previous results on uniaxially strained AGNRs, suggesting an interpretation based on the geometric deformation of the ribbon produced by the hydroxylation. However, tensile strain along the ribbon axis of 2 %, which is the maximum deviation of the lattice constant under functionalization, corresponds to a decrease of only 0.2 eV in the band-gap. Considering the extraordinarily high Poisson ratio caused by the OH passivation of the ribbon edges, we directly compare the variations in width and band-gap. The width reduction of 1.4 % observed for the fully functionalized 7-AGNR (see Fig. 7.3) would correspond to a tensile strain along the

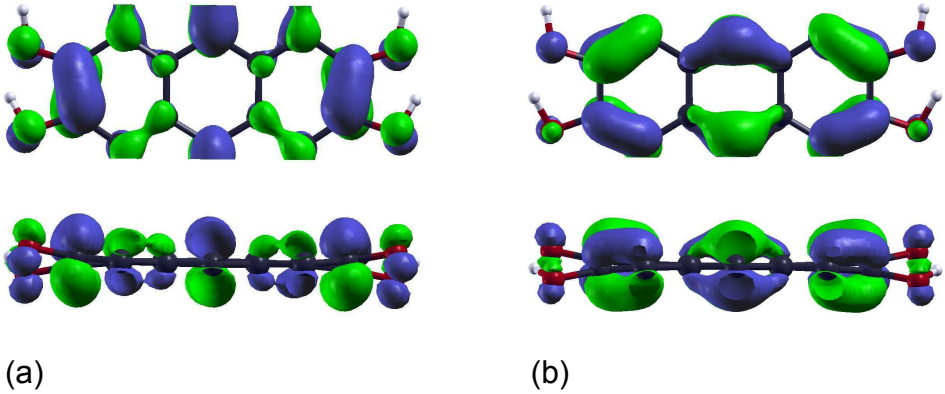

Figure 7.7: (a) Wave function of the highest π electronic state at the Γ point in a fully OH-functionalized 7-AGNR as seen from above the ribbon plane (top) and along the ribbon axis (bottom). The surfaces shown are given by a probability amplitude of 0.11 where green and blue areas denote different signs of the wave function. Atoms of different elements are shown in the same colors as in Fig. 7.1. (b) Γ point wave function of the lowest π^* state in the same ribbon.

ribbon axis of 5.6 %. This high strain value would give rise to a band-gap reduction of 0.6 eV which is close to the effect found for functionalized ribbons. When applying the same procedure to intermediate values of different degrees of functionalization, we find this trend being confirmed. In order to further check the role of deformation as an origin for the band-gap reduction, we calculate the band structure of an H-terminated ribbon, but with the carbon atoms being fixed at the altered positions corresponding to the fully functionalized case. This results in a more moderate reduction of the band-gap by only 0.4 eV, indicating that apart from the geometric deformation, another effect contributes to the change in the band-gap. It turns out that the substitution of OH groups affects the boundary condition of the electronic wave function. This is illustrated in Fig. 7.7 for the highest π and the lowest π^* orbital at the Γ point in a completely OH-functionalized 7-AGNR. Obviously, electrons in these states have a considerable probability density at the oxygen atoms in the functional groups. Thus, the quantum confinement close to the Fermi-level is weakened by the hydroxylation resulting in a lowered band-gap. We therefore conclude that a combination of geometric deformation and a reduced effective confinement potential gives rise to the observed strong reduction of the band-gap.
At this point, we want to refer to the family behavior of the band-gaps of strained AGNRs described in Sec. 6.2. In view of the crucial role of structural deformation in functionalized ribbons, one might expect that AGNRs of other families than that of the 7-AGNR show a contrary band-gap shift under hydroxylation. Our results presented in Fig. 7.8(a) indeed show an increasing gap under functionalization for N-AGNRs with $N = 3p$, whereas ribbons of the family $N = 3p+2$ have a minimal gap around a degree of functionalization of 0.4. In contrast, the band-gap of functionalized 10-AGNRs decreases

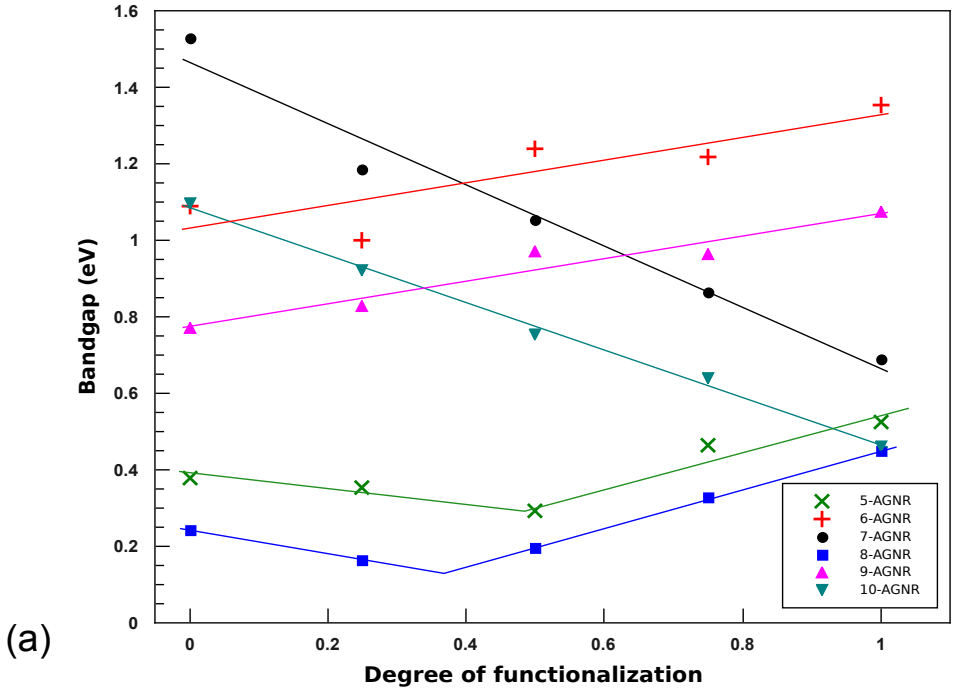

(a)

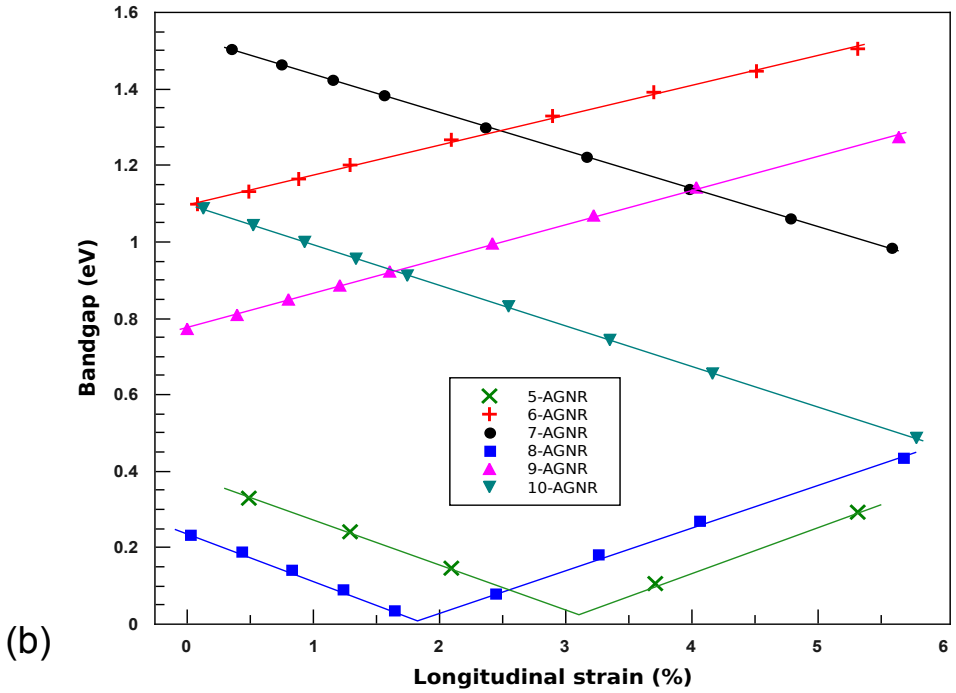

(b)

Figure 7.8: (a) Band-gaps of N-AGNRs with $N = 5, ..., 10$ depending on the degree of functionalization. (b) Dependence of the band-gaps of the same ribbons upon uniaxial strain. Solid lines are linear fits. For clarity, we only show results of the most stable configurations, *i.e.*, single-edge functionalized ribbons, at a degree of functionalization of 0.5 in (a) (*cf.* Sec. 7.2).

linearly in the same way as that of 7-AGNRs. These family behaviors match those found for the band-gaps of strained AGNRs, which are summarized in Fig. 7.8(b), very well. The strain ranges from 0 % to ~ 5.5 %, where the upper limit corresponds to the reduction of the ribbon width in the fully functionalized case, as stated above. The accordance in the patterns of functionalized and strained ribbons, respectively, clearly emphasizes that the main contribution to the band-gap variation in hydroxylated AGNRs is due to strain.

7.4 Vibrational spectrum

In the following, we investigate the behavior of the most important vibrational modes of AGNRs under different degrees of hydroxylation. We present data on the BLM and the LO and TO modes that dominate the Raman spectrum, as shown in Sec. 5.3. In addition, characteristic modes of the hydroxyl groups and the influence of the functionalization on the stretching modes of the remaining C-H bonds are discussed.

7.4.1 Breathing-like mode

In non-symmetric configurations with one or three OH groups per unit cell, the regular displacement pattern of the BLM can be distorted considerably by edge functionalization. Nevertheless, the basic breathing-like vibration is preserved in all investigated examples. Figure 7.9(a) shows the BLM frequency of various AGNRs depending on the degree of functionalization. As presented in Sec. 7.2, a degree of functionalization of 0.5 yields several inequivalent possibilities to arrange the OH groups. These configurations result in slightly different BLM frequencies. Nonetheless, since single edge functionalization is always energetically favorable, we neglect in the following discussions data from the other isomers and show, for clarity, only results of the thermodynamically most stable structure (*cf.* Fig. 7.4(b)).
Obviously, the addition of OH groups substantially damps the BLM in ribbons of all families, resulting in a red-shift of up to 160 cm^{-1} in case of the smallest studied ribbon, the 5-AGNR. As the BLM is Raman active, this huge down-shift allows the experimental determination of the degree of functionalization. It should be noted that in practice this goal may be hindered by the multitude of Raman active modes in less symmetric compounds. In Sec. 6.3, we showed that uniaxial strain also provokes a linear red-shift of the BLM. However, the dimension of the observed shift in functionalized AGNRs does not allow an exclusive ascription to the functionalization-induced strain even if we consider the unusually large Poisson ratio as described in Sec. 7.3. Most likely, multiple factors contribute to the strong frequency shift. Thus, the addition of functional groups to the ribbon edges may produce a similar effect as a broadening of the ribbon which is known to reduce the BLM frequency citegillen10. This assumption is supported by the displacement pattern of the BLM shown in Fig. 7.9(b). All atoms of the functional groups largely follow the breathing-like motion of the ribbon itself and vibrate in phase with the carbon atoms perpendicular to the ribbon axis and in the ribbon plane. Within the picture of an expanded ribbon structure, the oxygen atoms stand for an additional dimer

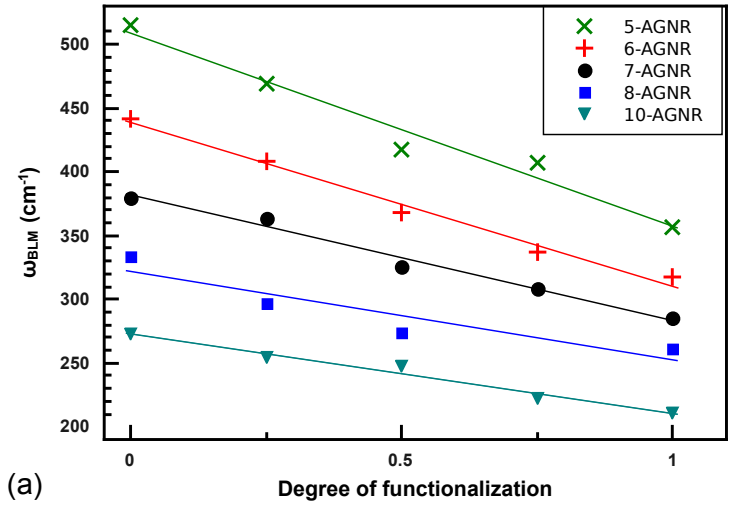

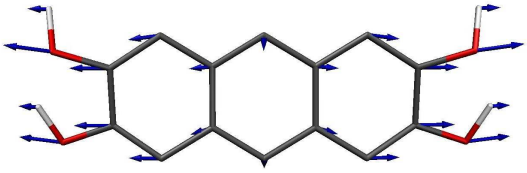

Figure 7.9: (a) Down-shift of the BLM for various hydroxyl-functionalized N-AGNRs. Solid lines are linear fits. (b) Eigenvector of the BLM of a fully hydroxylized 7-AGNR. Carbon, oxygen, and hydrogen atoms are shown in black, red, and light gray, respectively. Blue arrows indicate the atomic displacements.

at each edge of the ribbon. Thus, a fully functionalized N-AGNR can be thought of as a H-passivated $(N+2)$-AGNR. The BLM frequencies of the studied fully hydroxylized N-AGNRs are compared to those of their pristine, but two dimers wider counterparts, in Tab. 7.1. Given the rough underlying approximation and in view of the huge overall down-shift, the model explains the observed trend fairly well. Table 7.1 shows higher frequencies for the BLMs of pristine $(N+2)$-AGNRs, with a maximal deviation of $23\,\mathrm{cm}^{-1}$ in case of the 5-AGNR. This can be attributed to the fact that the heavier oxygen atoms in case of the functionalized ribbons damp the vibration compared to the equally wide AGNR consisting of carbon atoms only. Hence, we conclude that the large red-shift of the BLM can be attributed to both the functionalization-induced strain and an effective extension of the ribbon width by the hydroxyl groups.

N	$\omega_{N,\ \text{fully funct.}}$ (cm^{-1})	$\omega_{N+2,\ \text{non-funct.}}$ (cm^{-1})
5	357	380
6	317	334
7	285	300
8	261	273
10	211	230

Table 7.1: Frequency of the BLM in fully hydroxylized N-AGNRs and H-passivated $(N+2)$-AGNRs.

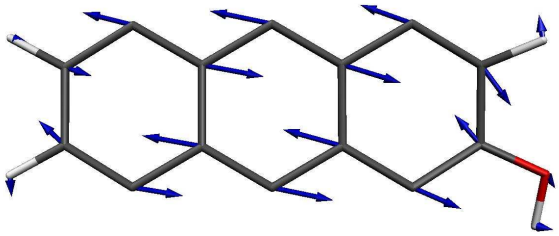

Figure 7.10: Displacement pattern of the TO mode in a 7-AGNR with one functional group per unit cell. The same color code as in Fig. 7.9(b) is used.

7.4.2 High energy band

As in case of the BLM, the eigenvectors of the LO and TO are distorted if the symmetry of the unit cell is limited by the addition of an odd number of OH groups. The example given in Fig. 7.10 shows that under this condition in particular, the carbon atoms do not vibrate purely along or perpendicular to the ribbon axis. However, the principle character of the phonons is well distinguishable in all structures examined here. Figure 7.11(a) displays the LO and TO frequencies of several AGNRs as a function of the degree of hydroxylation. As in Sec. 7.4.1, we do not take into account less stable isomers of single edge functionalized ribbons. For all AGNRs, we find a fundamentally different behavior of the two high-energy modes upon functionalization. Whereas the TO mode shifts to lower energies similar to the BLM, the LO frequency does not show such a clear trend. In N-AGNRs with $N = 3p$ and $N = 3p+1$, the LO seems to be independent of the edge passivation. In contrast, the $N = 3p+2$ family shows a declining LO frequency up to a degree of functionalization of 0.5, but a sharp blue-shift under hydroxylation of the remaining edge atoms. Interestingly, the condition under which the minimal LO energy is observed, coincides with that for a vanishing band-gap in this family (*cf.* Fig. 7.8(a)). This is in accordance with the significantly lowered LO frequency in pristine ribbons of the $N = 3p + 2$ family, which exhibit only small band-gaps [19, 88]. The correlation between lowered band-gap and softened LO energy is analogous to the softening of the LO frequency in metallic CNTs, which is interpreted in terms of an oscillating band-gap imposed by the specific atomic displacement of this phonon [69, 121]. Recently, it has been shown that the same Kohn anomaly effect as in CNTs plays an important role for the LO in quasi-metallic GNRs as well [113]. We therefore assume that the LO softening shown in Fig. 7.11(a) can be attributed to the same mechanism.
A different interpretation might be obtained when looking at the eigenvectors shown in Fig. 7.11(b). A noticeable difference between the two displacement patterns concerns the behavior of the functional groups. Whereas the oscillation of the carbon atoms in the TO eigenvector provokes a stretching of the C-O bonds, a strong bending of the OH group dominates the LO pattern. In both cases the motion of the outermost carbon atoms induces these characteristic vibrations of hydroxyl groups which are usually found at lower frequencies. Depending on the compound which is hydroxylized, in-plane deformations of the O-H groups are usually localized at 1260-1440 cm^{-1} and C-O stretching modes are found at 800-1150 cm^{-1} [122, 123]. The coupling of the TO to the low-energetic C-O stretching mode could potentially give rise to the observed softening of the TO frequency. In contrast, the C-O-H bending which couples to the LO is expected

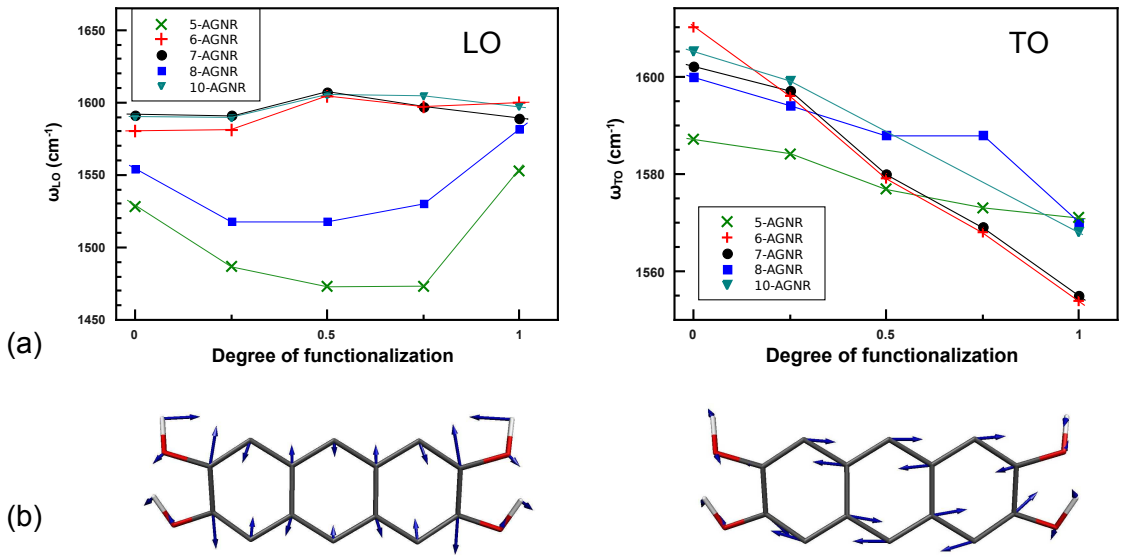

Figure 7.11: (a) Frequencies of the fundamentals of the LO (left) and TO phonons (right) of hydroxylized AGNRs. Solid lines are guides to the eye. (b) Eigenvectors of these modes in a fully functionalized 7-AGNR. Again, the same color code as in Fig. 7.9(b) is used.

to be closer in frequency to the LO-TO region. Therefore the LO should be affected less than the TO in agreement with our findings.

7.4.3 Vibrations of the functional groups

Finally, we discuss the high-energy range of the vibrational spectrum comprising the stretching modes of C-H and O-H bonds. We investigate these phonons taking the example of a 7-AGNR. All findings presented in the following also apply to ribbons of other widths, although the overall frequency range of the discussed modes varies depending on the specific type of AGNR.

A hydrogen-terminated AGNR yields two doubly degenerate pairs of C-H stretching vibrations. This number is reduced in functionalized ribbons to the number of remaining C-H bonds. Consequently we find as many O-H stretching modes as hydroxyl groups involved per unit cell. As displayed in Fig. 7.12(a), C-H stretching generally occurs in two narrow frequency ranges around 3000 and 3020 cm^{-1}. Figure 7.12(b) shows the three above-mentioned inequivalent structures with a degree of functionalization of 0.5. The two cases with one hydroxyl group per edge maintain C_2 rotational symmetry or, alternatively, a mirror plane. Hence, each of these configurations yields a doubly degenerate C-H stretching mode which is found at 2997 cm^{-1}. As expected, the non-symmetric single-edge hydroxylated 7-AGNR shows two separated C-H stretches. Measuring the C-H stretching frequencies would allow some insight in how many OH-groups are bound

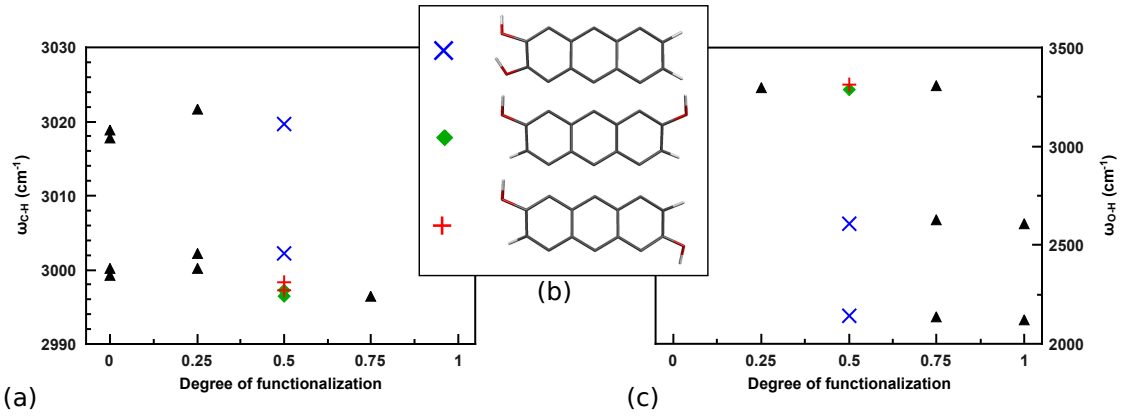

Figure 7.12: Stretching frequencies of (a) the C-H bonds and (c) the O-H bonds in 7-AGNRs depending on the degree of hydroxylation. Vibrational frequencies found for single-edge functionalization and the two different cases with half-functionalized edges are represented with the symbols stated in (b). (b) Three inequivalent configurations with two OH groups per unit cell. Different elements are again displayed in the color code of Fig. 7.9(b).

to the ribbon edges. From the absence of the modes at 3020 cm^{-1}, a high degree of functionalization may be deduced.
We now turn our attention to the O-H stretching vibrations presented in Fig. 7.12(c). Apart from the fully functionalized 7-AGNR, all configurations exhibit such modes around 3200 cm^{-1}. It turns out that these are vibrations of half functionalized edges, *i.e.*, of OH groups which do not have direct hydroxyl neighbors. As soon as a completely hydroxylized edge is involved, we observe a severe down-shift, which is a clear indication of hydrogen bonds. Opposite-phase stretching vibrations of neighboring OH groups are found at 2605 to 2630 cm^{-1}, whereas the corresponding in-phase modes are further lowered to 2120 to 2145 cm^{-1}. Accordingly the fully hydroxylized 7-AGNR does not show any OH-vibrations around 3200 cm^{-1}. The experimental detection of the O-H stretching modes thus allows to further narrow down the degree of functionalization of a given sample. Together with the results presented in Secs. 7.4.1 and 7.4.2, this suggests that an extensive characterization of hydroxyl-functionalized AGNRs is feasible via vibrational spectroscopy.

7.5 Summary

We presented a thorough investigation of the structural, electronic, and vibrational properties of AGNRs of various widths with hydroxyl-functionalized edges. The passivation of every carbon edge atom with an OH group gives the most stable configuration. At the same time, this maximum functionalization has the largest effect on the electronic band structure and on the main vibrational modes. The most striking result with regard to possible applications is the large linear shift of the band-gap which can be partially

attributed to strain induced by the hydroxylation. A tunable band-gap might be very useful in future nanometer-sized electronic devices. Finally, we showed that the degree of edge functionalization may be determined by Raman spectroscopy. These findings are particularly exciting in the light of the successful preparation of pure 7-AGNRs. An experimental verification of our results is thus within the realms of possibility. Moreover, in view of the enormous potential for chemical modifications at nanoribbon edges, it will be enlightening to further study the impact of other types of edge functionalization.

8 Conclusions

In this work, we studied fundamental characteristics of a variety of low-dimensional carbon allotropes by means of quantum mechanics based methods. The two main parts of this thesis dealt with carbon picotubes and different modifications of graphene nanoribbons. Most of the given structures were calculated using density-functional theory. A great advantage of this approach is that no experimental parameters are needed to model the materials of interest. In order to manage large systems – in our case compositions of a nanotube and several encapsulated picotubes – we complemented the *ab initio* method with semi-empirical calculations. These theoretical approaches allowed the investigation of arbitrary pristine materials which are inaccessible experimentally, *e.g.*, graphene nanoribbons other than some rare exceptions of precisely manufactured species like the 7-AGNR.

In the first part of this thesis, we studied substructures of narrow carbon nanotubes known as picotubes. Up to now, four different picotubes have been synthesized which correspond to the four smallest armchair nanotubes. Due to the structural resemblance to nanotubes, these ringlike molecules are considered to be possible starting points for a controlled synthesis of nanotubes. The close relationship between both materials is strongly reflected in the vibrational eigenmodes. We found radial breathing modes in all picotubes in direct correspondence to the same modes in nanotubes. Moreover, the picotube breathing vibrations satisfy the same frequency-diameter relation as the one known from nanotubes. Besides the radial breathing mode optical vibrations with atomic displacements longitudinal and transversal to the tube axis caught our attention. These modes, which are found at $\sim 1600\,\mathrm{cm}^{-1}$, are typical for sp^2 hybridized carbon materials. In nanotubes, optical phonons occur at similar energies and are widely used for characterization. Every picotube molecule exhibits a variety of such modes due to the reduced symmetry compared to nanotubes. We demonstrated that for two highly symmetric picotube species the longitudinal optical modes are not expected to contribute to the high-energy Raman spectrum. This behavior is in analogy to that of armchair nanotubes. By contrast, the Raman spectra of the two less symmetric picotubes are expected to show a wealth of longitudinal and optical contributions in accordance with experimental data.

With regard to a possible synthesis of closed nanotubes from picotubes we pursued an approach suggested by Schaman *et al.* which is based on the interaction of picotubes and nanotubes [26]. In that work, the authors present Raman data which points to a transformation of picotubes towards a short tubular configuration when the picotubes are placed next to or inside nanotubes. We performed temperature-dependent molecular dynamics simulations of tetramer picotubes encapsulated in a nanotube and found three independent effects. First, an ensemble of several consecutively arranged picotubes

shows oscillations or, in most cases, superpositions of rotational translational oscillations up to a temperature of 600 K. Secondly, we observe a continuous motion of the picotube molecules along the nanotube axis. The small energetic barrier for such a translation allows the transport of individual picotubes at very low temperatures. In contrast, a group of molecules shows a collective motion only above 800 K. Starting at temperatures of about 2500 K our calculations show structural conversions of the picotubes. In particular, a partial dehydrogenation leads to a closing of the separate picotube wings to a closed tubular wall. This finding confirms the work referred to above although the authors report the transformation to occur at lower temperatures. Further investigations could enlighten this issue since the experimental time-scale of one hour of annealing is not accessible within our approach. Possibly, longer simulation times might show a structural reconfiguration at lower temperatures. Optimizing various conditions like the temperature and the type of the surrounding nanotube might lead to a concatenation of the closed picotubes towards an inner nanotube of a predefined chirality. This remains an interesting task from both a theoretical and an experimental point of view.
The second part of this work dealt with graphene nanoribbons, a slightly different system which is related to carbon nanotubes by their common basic material graphene. Therefore, concepts like the zone-folding approximation can be applied to nanoribbons in a similar way as to nanotubes. Here, we investigated how strain on the one hand, and edge functionalization on the other hand affect the fundamental properties of nanoribbons. Our calculations on uniaxially strained armchair nanoribbons showed a severe impact on the band-gap. The same amount of strain leads to a widening of the gap in certain ribbons but a decreased gap in others. This behavior follows a classification of armchair nanoribbons into three distinct families reported earlier. A remarkable aspect is that the band-gap variation depends linearly on the applied strain with a shift rate of $\pm 0.1\,\mathrm{eV}/\%$ in all ribbons independent of the family. Furthermore, when considering a sufficiently large strain, the band-gap turns out to oscillate between zero and a maximum value. We interpreted these findings in terms of previous reports on the band structure of uniaxially strained graphene and found a good correspondence between the phenomena observed in both allotropes [108]. In addition to the electronic structure, high-energy and breathing-like phonons of strained nanoribbons were studied. We found linear frequency shifts for all of these vibrations in accordance with reports on the optical phonons in strained graphene. While the shift rate of the high-energy phonons is large enough to be made use of in the detection of strain, the shift of the breathing-like mode is much weaker and not likely to be exploited experimentally.
The edges of a nanoribbon are susceptible to a wide range of possible chemical modifications. Throughout the literature, hydrogen passivation of the dangling edge bonds is commonly assumed in order to describe pristine ribbons. The effect of functional groups has mainly been investigated in zigzag ribbons which exhibit edge states near the Fermi level. Nevertheless, functionalization is also a crucial issue in other types of ribbons as it can occur unintentionally during the manufacturing process or might be introduced on purpose in order to control certain ribbon characteristics. In order to provide a theoretical view on this topic, we performed calculations on armchair nanoribbons functionalized with hydroxyl groups. This type of passivation turns out to be particularly

stable although the ribbon structure is strained under the edge hydroxylation. We observed a significant influence of the functionalization on the band-gap which very much resembles the behavior of pristine strained ribbons. On closer inspection it turns out that, in addition, an effective softening of the lateral confinement potential of the electronic wave function plays an important role. A similar interpretation of a combination of strain and an effective broadening of the ribbon structure is proposed for explaining the observed red-shift of the breathing-like vibrational mode. Furthermore, we analyzed how the optical phonon frequencies depend on the degree of functionalization which revealed the following remarkable result: While the transversal modes of all ribbons show a continuous down-shift, the longitudinal phonons are softened only in those configurations that exhibit a vanishing band-gap. This is in accordance with a recent report on a Kohn-anomaly induced down-shift of the longitudinal optical phonon in quasi-metallic armchair nanoribbons [113]. Finally, we presented data on the vibrations of the hydroxyl groups that suggest a possible characterization of functionalized ribbons *via* these modes in Raman experiments.

In particular, our findings on the band structure of strained and hydroxylized nanoribbons are noteworthy with regard to future nanometer-sized electronic applications. Our results suggest that the band-gap of armchair graphene nanoribbons can be tuned to a desired value by means of mechanical or chemical modifications. However, it should be noted that this would require the availability of nanoribbons of a pristine edge configuration and width. This prerequisite is so far only fulfilled in the case of the 7-AGNR. Furthermore, as far as functionalization is concerned a precise control of the chemical reactions would be necessary as it is unclear how other functional groups will affect the ribbon characteristics. Further studies on this topic are to be performed to gain a more general insight into the wide field of possible edge passivations of nanoribbons.

Appendix: Symmetry of picotube vibrations

The symmetry of a molecular or crystalline system provides useful information about its vibrational properties. Including translations and rotations, a structure with N atoms per unit cell (or atoms contained in the molecule) exhibits $3N$ eigenmodes. These can be classified into categories of modes with eigenvectors of one type behaving identically with respect to the symmetry operations of the structure. In the group theoretical formalism, these categories are irreducible representations of the symmetry group [124,125]. Taking into account the permutation of the atoms under symmetry transformations, we can determine how many eigenmodes of each irreducible representation occur in a given system. Furthermore, symmetry determines whether modes behaving according to a certain representation are Raman active or not.
We start by analyzing the TDDA molecule, which belongs to the point group D_{2h} (see Sec. 3.1). A specific irreducible representation transforms with respect to the symmetry elements of the group according to a character table. These tables are found in books on group theory like Ref. [67], or [125]. For the group D_{2h} it is given in Tab. A.1. In order to describe the symmetry of molecular eigenmodes, information on the atomic displacements as well as on how the positions of the atoms are interchanged under symmetry operations is required. Thus, the dynamical representation Γ_{dyn}, which characterizes the vibrations of a system completely, can be expressed as the direct product of the vector representation and the permutation representation [67]:

$$\Gamma_{dyn} = \Gamma_{vec} \otimes \mathcal{P}. \tag{A.1}$$

Γ_{vec} is given by the direct sum of the irreducible representations describing the transformations of the components x, y, z. In the case of D_{2h} symmetry, this means

$$\Gamma_{vec} = B_{3u} \oplus B_{2u} \oplus B_{1u}, \tag{A.2}$$

as specified in Tab. A.1. $\mathcal{P}(R_i)$ is the matrix which permutes the atoms under the symmetry operation R_i. The character, which is defined as the trace of the representation matrix, is therefore given by the number of atom sites that are invariant with respect to R_i. The resulting characters for $\mathcal{P}$ in the case of TDDA are presented in the lowest line of Tab. A.1. Apart from the identity, only the horizontal mirror plane leaves some atom sites unchanged (*cf.* Fig. 3.3). Now the characters of Γ_{dyn} can be calculated as

$$\chi(\Gamma_{dyn}) = \chi(\Gamma_{vec}) \cdot \chi(\mathcal{P}). \tag{A.3}$$

Table A.1: Character table of the symmetry group D_{2h} taken from Ref. [125]. The last three lines show the characters of the vector (Γ_{vec}) and tensor ($\mathcal{R}$) representation and the permutation representation of TDDA ($\mathcal{P}$), all of which are reducible.

D_{2h}	E	C_2^z	C_2^y	C_2^x	i	$\sigma^{(xy)}$	$\sigma^{(xz)}$	$\sigma^{(yz)}$	
A_g	1	1	1	1	1	1	1	1	
B_{1g}	1	1	-1	-1	1	1	-1	-1	
B_{2g}	1	-1	1	-1	1	-1	1	-1	
B_{3g}	1	-1	-1	1	1	-1	-1	1	
A_u	1	1	1	1	-1	-1	-1	-1	
B_{1u}	1	1	-1	-1	-1	-1	1	1	z
B_{2u}	1	-1	1	-1	-1	1	-1	1	y
B_{3u}	1	-1	-1	1	-1	1	1	-1	x
Γ_{vec}	3	-1	-1	-1	-3	1	1	1	
$\mathcal{R}$	9	1	1	1	9	1	1	1	
$\mathcal{P}^{TDDA}$	44	0	0	0	0	4	0	0	

In order to obtain the molecular vibrations of TDDA, we decompose the (reducible) representation Γ_{dyn} into its irreducible components:

$$\Gamma_{dyn} = \sum_i c_i \Gamma_i, \tag{A.4}$$

with i labeling the irreducible representations. The coefficients c_i are given by

$$c_i = \frac{1}{g} \sum_j \chi_i(R_j) \chi^{(dyn)}(R_j), \tag{A.5}$$

where the sum is over all symmetry operations and g is the order of the group, *i.e.*, the number of symmetry elements. Evaluating these relations yields

$$\Gamma_{dyn}^{TDDA} = 17A_g \oplus 17B_{1g} \oplus 16B_{2g} \oplus 16B_{3g} \oplus 16A_u \oplus 16B_{1u} \oplus B_{2u} \oplus B_{3u}. \tag{A.6}$$

Let us now address the question which of these eigenmodes are expected to be Raman active. The Raman tensor is a second rank tensor and can thus be written as the outer product of two vectors. Therefore, we obtain the tensor representation from Γ_{vec} as

$$\mathcal{R} = \Gamma_{vec} \otimes \Gamma_{vec} \tag{A.7}$$

with the associated characters stated in Tab. A.1. In analogy to Eqs. A.4 and A.5, $\mathcal{R}$ can be reduced into irreducible representations:

$$\mathcal{R}^{TDDA} = 3A_g \oplus 2B_{1g} \oplus 2B_{2g} \oplus 2B_{3g}. \tag{A.8}$$

Table A.2: Character table of the symmetry group D_{2h} taken from Ref. [125]. Again, the last three lines show the (reducible) vector and tensor representation as well as the permutation representation of Kammermeierphane.

C_{2h}	E	C_2	i	σ_h	
A_g	1	1	1	1	
A_u	1	1	-1	-1	z
B_g	1	-1	1	-1	
B_u	1	-1	-1	1	x,y
Γ_{vec}	3	-1	-3	1	
$\mathcal{R}$	9	1	9	1	
$\mathcal{P}^{KP}$	96	0	0	0	

Only the eigenmodes transforming according to these representations are Raman active. Table A.1 shows that this comprises precisely those vibrations which are invariant under inversion. This has been proved to be a general rule in molecules [67]. The forms of the Raman tensors corresponding to the different representations are given in Ref. [126]. Note that Raman activity is determined purely by symmetry and therefore independent of the specific system.

An analogous investigation can be done for Kammermeierphane, which belongs to the point group C_{2h}. The character table of this group together with the characters of the representations Γ_{vec}, $\mathcal{R}$, and $\mathcal{P}$ is presented in Tab. A.2. The dynamical representation of Kammermeierphane contains 72 eigenmodes of each of the four irreducible representations, respectively. The tensor representation decomposes to

$$\mathcal{R}^{KP} = 5A_g \oplus 4B_g \tag{A.9}$$

thus confirming the Raman activity of modes which are invariant under inversion.
As far as the selection rules of semitrimer and tetramer picotubes are concerned the reader is referred to Refs. [52, 54, 127].

Bibliography

[1] R. Fort and P. Schleyer, "Adamantane - consequences of diamondoid structure", Chem. Rev. **64**, 277 (1964).

[2] J. E. Dahl, S. G. Liu, and R. M. K. Carlson, "Isolation and structure of higher diamondoids, nanometer-sized diamond molecules", Science **299**, 96 (2003).

[3] H. W. Kroto, J. R. Heath, S. C. O'Brien, R. F. Curl, and R. E. Smalley, "C_{60}: Buckminsterfullerene", Nature **318**, 162 (1985).

[4] S. Iijima, "Helical microtubules of graphitic carbon", Nature **354**, 56 (1991).

[5] K. S. Novoselov, A. K. Geim, S. V. Morozov, D. Jiang, Y. Zhang, *et al.*, "Electric field effect in atomically thin carbon films", Science **306**, 666 (2004).

[6] P. G. Collins and P. Avouris, "Nanotubes for electronics", Sci. Am. **283**, 62 (2000).

[7] S. Berber, Y.-K. Kwon, and D. Tománek, "Unusually high thermal conductivity of carbon nanotubes", Phys. Rev. Lett. **84**, 4613 (2000).

[8] C. Lee, X. Wei, J. W. Kysar, and J. Hone, "Measurement of the elastic properties and intrinsic strength of monolayer graphene", Science **321**, 385 (2008).

[9] A. A. Balandin, S. Ghosh, W. Bao, I. Calizo, D. Teweldebrhan, F. Miao, and C. N. Lau, "Superior thermal conductivity of single-layer graphene", Nano Lett. **8**, 902 (2008).

[10] J. W. Mintmire, B. I. Dunlap, and C. T. White, "Are fullerene tubules metallic?", Phys. Rev. Lett. **68**, 631 (1992).

[11] T. Dürkop, S. A. Getty, E. Cobas, and M. S. Fuhrer, "Extraordinary mobility in semiconducting carbon nanotubes", Nano Lett. **4**, 35 (2004).

[12] X. Du, I. Skachko, A. Barker, and E. Y. Andrei, "Approaching ballistic transport in suspended graphene", Nature Nanotech. **3**, 491 (2008).

[13] S. Reich, C. Thomsen, and J. Maultzsch, *Carbon Nanotubes, Basic Concepts and Physical Properties* (Wiley-VCH, Berlin, 2004).

[14] M. Zheng, A. Jagota, M. S. Strano, A. P. Santos, P. Barone, *et al.*, "Structure-based carbon nanotube sorting by sequence-dependent DNA assembly", Science **302**, 1545 (2003).

[15] M. S. Arnold, A. A. Green, J. F. Hulvat, S. I. Stupp, and M. C. Hersam, "Sorting carbon nanotubes by electronic structure using density differentiation", Nat. Nanotechnol. **1**, 60 (2006).

[16] R. Herges, "Mit rationaler synthese zu kohlenstoff-nanotubes", Nachrichten aus der Chemie **55**, 962 (2007).

[17] S. Kammermeier, P. G. Jones, and R. Herges, "Ring-expanding metathesis of tetradehydrodianthracene - synthesis and structure of a tubelike, fully conjugated hydrocarbon", Angew. Chem. Int. Ed. Eng. **35**, 2669 (1996).

[18] K. Nakada, M. Fujita, G. Dresselhaus, and M. S. Dresselhaus, "Edge state in graphene ribbons: Nanometer size effect and edge shape dependence", Phys. Rev. B **54**, 17 954 (1996).

[19] Y.-W. Son, M. L. Cohen, and S. G. Louie, "Energy gaps in graphene nanoribbons", Phys. Rev. Lett. **97**, 216 803 (2006).

[20] A. Betti, G. Fiori, and G. Iannaccone, "Strong mobility degradation in ideal graphene nanoribbons due to phonon scattering", Appl. Phys. Lett. **98**, 212 111 (2011).

[21] J. Cai, P. Ruffieux, R. Jaafar, M. Bieri, T. Braun, *et al.*, "Atomically precise bottom-up fabrication of graphene nanoribbons", Nature **466**(7305), 470 (2010).

[22] O. Hod, V. Barone, J. E. Peralta, and G. E. Scuseria, "Enhanced half-metallicity in edge-oxidized zigzag graphene nanoribbons", Nano Lett. **7**(8), 2295 (2007).

[23] T. Wassmann, A. P. Seitsonen, A. M. Saitta, M. Lazzeri, and F. Mauri, "Structure, stability, edge states, and aromaticity of graphene ribbons", Phys. Rev. Lett. **101**, 096 402 (2008).

[24] F. Cervantes-Sodi, G. Csanyi, S. Piscanec, and A. C. Ferrari, "Edge-functionalized and substitutionally doped graphene nanoribbons: Electronic and spin properties", Phys. Rev. B **77**(16), 165 427 (2008).

[25] B. W. Smith, M. Monthioux, and D. E. Luzzi, "Encapsulated C_{60} in carbon nanotubes", Nature **396**, 323 (1998).

[26] C. Schaman, R. Pfeiffer, V. Zólyomi, H. Kuzmany, D. Ajami, *et al.*, "The transformation of open picotubes to a closed molecular configuration", Phys. Status Solidi (B) **243**, 3151 (2006).

[27] N. W. Ashcroft and N. D. Mermin, *Solid State Physics* (Saunder College Publishers, 1976).

[28] P. Hohenberg and W. Kohn, "Inhomogeneous electron gas", Phys. Rev. B **136**, 864 (1964).

[29] W. Kohn, "Nobel lecture: Electronic structure of matter–wave functions and density functionals", Rev. Mod. Phys. **71**, 1253 (1999).

[30] W. Kohn and L. J. Sham, "Self-consistent equations including exchange and correlation effects", Phys. Rev. A **140**, 1133 (1965).

[31] W. Kohn, A. D. Becke, and R. G. Parr, "Density functional theory of electronic structure", J. Phys. Chem. **100**, 12 974 (1996).

[32] E. P. Wigner, "Effects of the electron interaction on the energy levels of electrons in metals", Trans. Faraday Soc. **34**, 678 (1938).

[33] M. Gell-Mann and K. A. Brueckner, "Correlation energy of an electron gas at high density", Phys. Rev. **106**, 364 (1957).

[34] D. M. Ceperley and B. J. Alder, "Ground state of an electron gas by a stochastic method", Phys. Rev. Lett. **45**, 566 (1981).

[35] M. S. Hybertsen and S. G. Louie, "Electron correlation in semiconductors and insulators: Band gaps and quasiparticle energies", Phys. Rev. B **34**, 5390 (1986).

[36] P. Ordejón, E. Artacho, and J. M. Soler, "Self-consistent order-N density-functional calculations for very large systems", Phys. Rev. B **53**, 10 441(R) (1996).

[37] E. Artacho, D. Sánchez-Portal, P. Ordejón, A. García, and J. Soler, "Linear-scaling ab-initio calcluations for large and complex systems", Phys. Status Solidi (B) **215**, 809 (1999).

[38] J. M. Soler, E. Artacho, J. D. Gale, A. García, J. Junquera, P. Ordejón, and D. Sánchez-Portal, "The SIESTA method for *ab initio* order-N materials simulation", J. Phys.: Condens. Matter. **14**, 2745 (2002).

[39] D. R. Hamann, M. Schlüter, and C. Chiang, "Norm-conserving pseudopotentials", Phys. Rev. Lett. **43**, 1494 (1979).

[40] M. C. Payne, M. P. Teter, D. C. Allan, T. A. Arias, and J. D. Joannopoulos, "Iterative minimization techniques for ab initio total-energy calculations: molecular dynamics and conjugate gradients", Rev. Mod. Phys. **64**, 1045 (1992).

[41] J. Junquera, O. Paz, D. Sánchez-Portal, and E. Artacho, "Numerical atomic orbitals for linear-scaling calculations", Phys. Rev. B **64**, 235 111 (2001).

[42] M. R. Hestenes and E. Stiefel, "Methods of conjugate gradients for solving linear systems", J. Res. Natl. Inst. Stan. **49**, 409 (1952).

[43] P. Ordejón, D. A. Drabold, R. M. Martin, and S. Itoh, "Linear scaling method for phonon calculations from electronic structure", Phys. Rev. Lett. **75**, 1324 (1995).

[44] E. Artacho, E. Anglada, O. Diéguez, J. D. Gale, A. García, *et al.*, "The SIESTA method; developments and applicability", J. Phys.: Condens. Matter **20**, 064 208 (2008).

[45] M. J. S. Dewar and W. Thiel, "Ground states of molecules. 38. the mndo method. approximations and parameters", Journal of the American Chemical Society **99**, 4899 (1977).

[46] F. Jensen, *Introduction to Computational Chemistry* (Wiley & Sons Ltd., Chichester, 2007).

[47] M. J. S. Dewar, E. G. Zoebisch, E. F. Healy, and J. J. P. Stewart, "AM1: a new general purpose quantum mechanical molecular model", J. Am. Chem. Soc. **107**, 3902 (1985).

[48] J. J. P. Stewart, "Optimization of parameters for semiempirical methods i. method", J. Comput. Chem. **10**, 209 (1989).

[49] M. Field, *A Practical Introduction to the Simulation of Molecular Systems* (Cambridge University Press, Cambridge, 2007).

[50] M. Field, "The pDynamo Program for Molecular Simulations using Hybrid Quantum Chemical and Molecular Mechanical Potentials", J. Chem. Theory Comput. **4**, 1151 (2008).

[51] W. C. Swope, H. C. Andersen, P. H. Berens, and K. R. Wilson, "A computer simulation method for the calculation of equilibrium constants for the formation of physical clusters of molecules: Application to small water clusters", J. Chem. Phys. **76**, 637 (1982).

[52] N. Rosenkranz, M. Machón, R. Herges, and C. Thomsen, "Vibrational properties of semitrimer picotubes", Chem. Phys. Lett. **451**, 249 (2008).

[53] N. Rosenkranz, M. Machón, R. Herges, and C. Thomsen, "Vibrational properties of four consecutive carbon picotubes", Phys. Status Solidi (B) **245**, 2145 (2008).

[54] M. Machón, S. Reich, J. Maultzsch, R. Herges, and C. Thomsen, "Structural, electronic, and vibrational properties of (4,4) picotube crystals", Phys. Rev. B **72**, 155 402 (2005).

[55] S. Kammermeier, P. G. Jones, and R. Herges, "Beltlike aromatic hydrocarbons by metathesis reaction with tetradehydrodianthracene", Angew. Chem. Int. Ed. Eng. **36**, 2200 (1997).

[56] R. L. Viavattene, F. D. Greene, L. D. Cheung, R. Majeste, and L. M. Trefonas, "9,9',10,10'-Tetradehydrodianthracene. Formation, protection, and regeneration of a strained double bond", J. Am. Chem. Soc. **96**, 4342 (1974).

[57] S. Kammermeier and R. Herges, "Photochemically induced metathesis reactions of tetradehydrodianthracene: Synthesis and structure of bianthraquinodimethane", Angew. Chem. Int. Ed. Eng. **35**, 417 (1996).

[58] L. T. Scott, "Conjugated belts and nanorings with radially oriented p orbitals", Angew. Chem. Int. Ed. **42**, 4133 (2003).

[59] M. Machón, S. Reich, C. Thomsen, D. Sánchez-Portal, and P. Ordejón, "*Ab initio* calculations of the optical properties of 4-Å-diameter single-walled nanotubes", Phys. Rev. B **66**, 155 410 (2002).

[60] R. Herges *et al.*, to be published.

[61] M. Budyka, T. Zyubina, A. Ryabenko, S. Lin, and A. Mebel, "Bond lengths and diameters of armchair single wall carbon nanotubes", Chem. Phys. Lett. **407**, 266 (2005).

[62] R. Herges, private communication.

[63] H. Telg, J. Maultzsch, S. Reich, F. Hennrich, and C. Thomsen, "Chirality distribution and transition energies of carbon nanotubes", Phys. Rev. Lett. **93**, 177 401 (2004).

[64] J. Kürti, G. Kresse, and H. Kuzmany, "First-principles calculations of the radial breathing mode of single-wall nanotubes", Phys. Rev. B **58**, 8869 (1998).

[65] J. Maultzsch, H. Telg, S. Reich, and C. Thomsen, "Radial breathing mode of single-walled carbon nanotubes: Optical transition energies and chiral-index assignment", Phys. Rev. B **72**, 205 438 (2005).

[66] J. Kürti, V. Zólyomi, M. Kertesz, and G. Sun, "The geometry and the radial breathing mode of carbon nanotubes: beyond the ideal behaviour", New. J. Phys **5**, 125 (2003).

[67] M. S. Dresselhaus, G. Dresselhaus, and A. Jorio, *Group Theory: Application to the Physics of Condensed Matter* (Springer-Verlag, Berlin, Heidelberg, 2008).

[68] C. N. Banwell, *Fundamentals of Molecular Spectroscopy* (McGraw-Hill, Maidenhead, 1972).

[69] O. Dubay, G. Kresse, and H. Kuzmany, "Phonon softening in metallic nanotube by a Peierls-like mechanism", Phys. Rev. Lett. **88**, 235 506 (2002).

[70] H. Farhat, H. Son, G. G. Samsonidze, S. Reich, M. S. Dresselhaus, and J. Kong, "Phonon softening in individual metallic carbon nanotubes due to the kohn anomaly", Phys. Rev. Lett. **99**, 145 506 (2007).

[71] N. Rosenkranz and C. Thomsen, "Molecular dynamics simulations of picotube peapods", Phys. Status Solidi (B) **246**, 2622 (2009).

[72] H. Kataura, Y. Maniwa, T. K. K. Kikuchi, K. Hirahara, S. Iijima, *et al.*, "Fullerene-peapods: Synthesis, structure, and raman spectroscopy", in *Proceedings of the XVth International Winterschool on Electronic Properties of Novel Materials* (2001), vol. 591 of *AIP Conference Proceedings*, p. 251.

[73] R. Saito, R. Matsuo, T. Kimura, G. Dresselhaus, and M. Dresselhaus, "Anomalous potential barrier of double-wall carbon nanotube", Chem. Phys. Lett. **348**, 187 (2001).

[74] L. Ci, Z. Rao, Z. Zhou, D. Tang, X. Yan, *et al.*, "Double wall carbon nanotubes promoted by sulfur in a floating iron catalyst cvd system", Chem. Phys. Lett. **359**, 63 (2002).

[75] K. Kelly, I. Chiang, E. Mickelson, R. Hauge, J. Margrave, *et al.*, "Insight into the mechanism of sidewall functionalization of single-walled nanotubes: an STM study", Chem. Phys. Lett. **313**, 445 (1999).

[76] E. V. Basiuk, M. Monroy-Peláez, I. Puente-Lee, and V. A. Basiuk, "Direct solvent-free amination of closed-cap carbon nanotubes: A link to fullerene chemistry", Nano Lett. **4**, 863 (2004).

[77] C. Fantini, E. Cruz, A. Jorio, M. Terrones, H. Terrones, *et al.*, "Resonance raman study of linear carbon chains formed by the heat treatment of double-wall carbon nanotubes", Phys. Rev. B **73**, 193 408 (2006).

[78] M. Whitby and N. Quirke, "Fluid Flow in Carbon Nanotubes and Nanopipes", Nature Nanotech. **2**, 87 (2007).

[79] S. Joseph, R. J. Mashl, E. Jakobsson, and N. R. Aluru, "Electrolytic Transport in Modified Carbon Nanotubes", Nano Lett. **3**, 1399 (2003).

[80] P. A. E. Schoen, J. H. Walther, S. Arcidiacono, D. Poulikakos, and P. Koumoutsakos, "Nanoparticle Traffic on Helical Tracks: Thermophoretic Mass Transport through Carbon Nanotubes", Nano Lett. **6**, 1910 (2006).

[81] J.-C. Charlier and J.-P. Michenaud, "Energetics of multilayered carbon tubules", Phys. Rev. Lett. **70**, 1858 (1993).

[82] N. Rosenkranz, M. Mohr, and C. Thomsen, "Uniaxial strain in graphene and armchair graphene nanoribbons: An *ab initio* study", Ann. Phys. **523**, 137 (2011).

[83] N. Rosenkranz, C. Till, C. Thomsen, and J. Maultzsch, "*Ab initio* calculations of edge-functionalized armchair graphene nanoribbons: Structural, electronic, and vibrational effects", Phys. Rev. B **84**, 195 438 (2011).

[84] P. R. Wallace, "The band theory of graphite", Phys. Rev. **71**, 622 (1947).

[85] A. K. Geim and K. S. Novoselov, "The rise of graphene", Nat. Mat. **6**, 183 (2007).

[86] A. H. C. Neto, F. Guinea, N. M. R. Peres, K. S. Novoselov, and A. K. Geim, "The electronic properties of graphene", Rev. Mod. Phys. **81**, 109 (2009).

[87] K. S. Novoselov, Z. Jiang, Y. Zhang, S. V. Morozov, H. L. Stormer, *et al.*, "Room-temperature quantum hall effect in graphene", Science **315**, 1379 (2007).

[88] V. Barone, O. Hod, and G. E. Scuseria, "Electronic structure and stability of semiconducting graphene nanoribbons", Nano Lett. **6**, 2748 (2006).

[89] X. Wang, Y. Ouyang, X. Li, H. Wang, J. Guo, and H. Dai, "Room-temperature all-semiconducting sub-10-nm graphene nanoribbon field-effect transistors", Phys. Rev. Lett. **100**, 206 803 (2008).

[90] Z. Xu, Q.-S. Zheng, and G. Chen, "Elementary building blocks of graphene-nanoribbon-based electronic devices", Appl. Phys. Lett. **90**, 223 115 (2007).

[91] B. Huang, Q. Yan, Z. Li, and W. Duan, "Towards graphene nanoribbon-based electronics", Front. Phys. China **4**, 296 (2009).

[92] S. Neubeck, Y. M. You, Z. H.Ni, P. Blake, Z. X. Shen, A. K. Geim, and K. S. Novoselov, "Direct determination of the crystallographic orientation of graphene edges by atomic resolution imaging", Appl. Phys. Lett. **97**, 053 110 (2010).

[93] Ç. Ö. Girit, J. C. Meyer, R. Erni, M. D. Rossell, C. Kisielowski, *et al.*, "Graphene at the edge: Stability and dynamics", Science **323**, 1705 (2009).

[94] M. Y. Han, B. Özyilmaz, Y. Zhang, and P. Kim, "Energy band-gap engineering of graphene nanoribbons", Phys. Rev. Lett. **98**, 206 805 (2007).

[95] X. Li, X. Wang, L. Zhang, S. Lee, and H. Dai, "Chemically derived, ultrasmooth graphene nanoribbon semiconductors", Science **319**, 1229 (2008).

[96] Z.-S. Wu, W. Ren, L. Gao, B. Liu, J. Zhao, and H.-M. Cheng, "Efficient synthesis of graphene nanoribbons sonochemically cut from graphene sheets", Nano Res. **3**, 16 (2010).

[97] D. V. Kosynkin, A. L. Higginbotham, A. Sinitskii, J. R. Lomeda, A. Dimiev, B. K. Price, and J. M. Tour, "Longitudinal unzipping of carbon nanotubes to form graphene nanoribbons", Nature **458**, 872 (2009).

[98] L. Jiao, L. Zhang, X. Wang, G. Diankov, and H. Dai, "Narrow graphene nanoribbons from carbon nanotubes", Nature **458**, 877 (2009).

[99] K. Kim, A. Sussman, and A. Zettl, "Graphene nanoribbons obtained by electrically unwrapping carbon nanotubes", .

[100] X. Jia, M. Hofmann, V. Meunier, B. G. Sumpter, J. Campos-Delgado, *et al.*, "Controlled formation of sharp zigzag and armchair edges in graphitic nanoribbons", Science **323**, 1701 (2009).

[101] Y.-W. Son, M. L. Cohen, and S. G. Louie, "Half-metallic graphene nanoribbons", Nature **444**, 347 (2006).

[102] A. C. Ferrari, J. C. Meyer, V. Scardaci, C. Casiraghi, M. Lazzeri, *et al.*, "Raman spectrum of graphene and graphene layers", Phys. Rev. Lett. **97**, 187 401 (2006).

[103] O. Frank, M. Mohr, J. Maultzsch, C. Thomsen, I. Riaz, *et al.*, "Raman 2D-band splitting in graphene: Theory and experiment", ACS Nano **5**, 2231 (2011).

[104] R. Gillen, M. Mohr, C. Thomsen, and J. Maultzsch, "Vibrational properties of graphene nanoribbons by first-principles calculations", Phys. Rev. B **80**, 155 418 (2009).

[105] J. Zhou and J. Dong, "Radial breathing-like mode of wide carbon nanoribbon", Phys. Lett. A **372**, 7183 (2008).

[106] R. Gillen, M. Mohr, and J. Maultzsch, "Symmetry properties of vibrational modes in graphene nanoribbons", Phys. Rev. B **81**, 205 426 (2010).

[107] J. Zhou and J. Dong, "Vibrational property and raman spectrum of carbon nanoribbon", Appl. Phys. Lett. **91**, 173 108 (2007).

[108] M. Mohr, K. Papagelis, J. Maultzsch, and C. Thomsen, "Two-dimensional electronic and vibrational band structure of uniaxially strained graphene from ab initio calculations", Phys. Rev. B **80**, 205 410 (2009).

[109] E. McCann, K. Kechedzhi, V. I. Fal'ko, H. Suzuura, T. Ando, and B. L. Altshuler, "Weak-localization magnetoresistance and valley symmetry in graphene", Phys. Rev. Lett. **97**(14) (2006).

[110] L. Yang, M. L. Cohen, and S. G. Louie, "Excitonic effects in the optical spectra of graphene nanoribbons", Nano Lett. **7**, 3112 (2007).

[111] D. Prezzi, D. Varsano, A. Ruini, A. Marini, and E. Molinari, "Optical properties of graphene nanoribbons: The role of many-body effects", Phys. Rev. B **77**, 041 404 (2008).

[112] Y. Lu and J. Guo, "Band gap of strained graphene nanoribbons", Nano Res. **3**, 189 (2010).

[113] K.-I. Sasaki, M. Yamamoto, S. Murakami, R. Saito, M. S. Dresselhaus, *et al.*, "Kohn anomalies in graphene nanoribbons", Phys. Rev. B **80**, 155 450 (2009).

[114] P. Giannozzi, S. Baroni, N. Bonini, M. Calandra, R. Car, *et al.*, "Quantum espresso: a modular and open-source software project for quantum simulations of materials", J. Phys.: Condens. Matter **21**, 395 502 (2009).

[115] F. Favot and A. Dal Corso, "Phonon dispersions: Performance of the generalized gradient approximation", Phys. Rev. B **60**, 11 427 (1999).

[116] A. Sinitskii and J. M. Tour, "Patterning graphene nanoribbons using copper oxide nanowires", Appl. Phys. Lett. **100**(10), 103 106 (2012).

[117] G. Lee and K. Cho, "Electronic structures of zigzag graphene nanoribbons with edge hydrogenation and oxidation", Phys. Rev. B **79**(16), 165 440 (2009).

[118] D. Boukhvalov, "Repair of magnetism in oxidized graphene nanoribbons", Chemical Physics Letters **501**, 396 (2011).

[119] M. Vanin, J. Gath, K. S. Thygesen, and K. W. Jacobsen, "First-principles calculations of graphene nanoribbons in gaseous environments: Structural and electronic properties", Phys. Rev. B **82**, 195 411 (2010).

[120] P. Wagner, C. P. Ewels, V. V. Ivanovskaya, P. R. Briddon, A. Pateau, and B. Humbert, "Ripple edge engineering of graphene nanoribbons", Phys. Rev. B **84**, 134 110 (2011).

[121] S. Piscanec, M. Lazzeri, J. Robertson, A. C. Ferrari, and F. Mauri, "Optical phonons in carbon nanotubes: Kohn anomalies, peierls distortions, and dynamic effects", Phys. Rev. B **75**, 035 427 (2007).

[122] D. Lin-Vien, N. B. Colthup, W. G. Fateley, and J. G. Grasselli, *The Handbook of Infrared and Raman Characteristic Frequencies of Organic Molecules* (Academic Press Inc., 1991).

[123] G. Socrates, *Infrared and Raman Characteristic Group Frequencies* (Wiley and Sons Ltd., 2001).

[124] J. W. Leech and D. J. Newman, *How to use groups* (Methuen & Co. Ltd., London, 1969).

[125] M. Wagner, *Gruppentheoretische Methoden in der Physik* (Vieweg Verlag, Braunschweig, Wiesbaden, 1998).

[126] M. Cardona, "Resonance phenomena", in *Light Scattering in Solids II*, edited by M. Cardona and G. Güntherodt (Springer, Berlin, 1982).

[127] M. Machón, *Electron-phonon coupling, vibrational and optical properties of carbon nanotubes and picotubes*, Ph.D. thesis, Technische Universität Berlin (2006).

Acknowledgments

This work would not have been possible without the contribution of many people. Especially, I would like to thank ...

Christian Thomsen for being my supervisor, for giving me the chance to work in his wonderful group, for his enthusiasm for all kinds of physical problems, and for the granted freedom in organizing my research activities. I have come to very much appreciate his optimistic and yet pragmatic attitude and his ability to encourage people.

Milan Damnjanović for reviewing this thesis, for the kind invitations to his group, for his interest in my work, and for many enlightening conversations on both physics and non-scientific issues. I really enjoyed the nice time in Belgrade and at the conference in Drvengrad.

Michael Lehmann for being the chairman of my thesis committee.

Janina Maultzsch for advising me on many occasions, for always finding time to answer my questions in spite of her busy schedule, and for giving an excellent course on the basics of group theory.

María Machón for teaching me the fundamentals of scientific work and writing, the ins and outs of publishing and numerous related topics, and for advising me beyond my Diploma thesis. I particularly enjoyed our long discussions on pretty much everything.

Marcel Mohr for a lot of help with problems related to SIESTA, for maintaining the cluster, and for proof-reading parts of this thesis.

my office mates Hagen Telg and Andrei Schliwa for an excellent working atmosphere and for finding a sound balance between concentration and creative breaks. Special thanks to Hagen Telg for convincing me of the advantages of Linux.

Harald Scheel, Asmus Vierck, and Dirk Heinrich for their technical support on cluster administration and on all kinds of hardware trouble as well as for relaxing conversations about non-physics topics.

Sabine Morgner, Marianne Heinold (†), Mandy Neumann, and Anja Sandersfeld for their professional help on bureaucratic problems and teaching issues and for spreading good humor.

Patrick May, Matthias Müller, Holger Lange, Jan Laudenbach, Matthias Staiger, and Felix Herziger for many helpful and inspiring discussions. Special thanks to Patrick May for extensive proof-reading.

Christian Till for being my bachelor's and master's student and for fruitful discussions about nanoribbons, SIESTA, education, *etc.*

all members of the groups of Christian Thomsen, Janina Maultzsch, and Axel Hoffmann for a unique working environment. In addition to a lively scientific exchange, this was promoted by events such as the nice Tischtennisplatten-meetings and common sports activities. Many thanks also for memorable shared experiences at various conferences.

my parents for their continuous support, especially in encouraging me to follow the route to world of science.

Helena and Clara for providing the greatest imaginable support.